OPTICAL FIBER BASED ULTRASHORT PULSE MULTISPECTRAL NONLINEAR OPTICAL MICROSCOPY

A Dissertation

by

ADAM M. LARSON

Submitted to the Office of Graduate Studies of
Texas A&M University
in partial fulfillment of the requirements for the degree of

DOCTOR OF PHILOSOPHY

December 2008

Major Subject: Biomedical Engineering

OPTICAL FIBER BASED ULTRASHORT PULSE MULTISPECTRAL NONLINEAR OPTICAL MICROSCOPY

A Dissertation

by

ADAM M. LARSON

Submitted to the Office of Graduate Studies of
Texas A&M University
in partial fulfillment of the requirements for the degree of

DOCTOR OF PHILOSOPHY

Approved by:

Chair of Committee,	Alvin T. Yeh
Committee Members,	Robert Burghardt
	Gerard Coté
	Kenith E. Meissner
Head of Department,	Gerard Coté

December 2008

Major Subject: Biomedical Engineering

ABSTRACT

Optical Fiber Based Ultrashort Pulse Multispectral
Nonlinear Optical Microscopy. (December 2008)
Adam M. Larson, B.S., University of Rochester
Chair of Advisory Committee: Dr. Alvin T. Yeh

Nonlinear optical microscopy (NLOM) utilizing femtosecond laser pulses is well suited for imaging living tissues. This work reports on the design and development of an optical fiber based multispectral NLOM developed around a laser generating broadband sub-10-fs pulses. An all-mirror dispersion-compensation setup is used to correct for quadratic and cubic phase distortions induced within the NLOM. Mouse tail tendon was used to characterize sub-10-fs pulses by interferometric autocorrelation. This is an effective method for characterizing dispersion from the optical system, immersion medium, and wet biological sample. The generation of very short autocorrelations demonstrates the ability to compensate for phase distortions within the imaging system and efficient second-harmonic upconversion of the ultrashort pulse spectrum within collagen. Reconstruction of ultrashort pulses at the focal plane of the objective allows the excitation of multiple fluorescent probes simultaneously. Multiple fluorescent probe excitation and spectral discrimination is demonstrated using mixtures of fluorescent dye solutions and an *in-vitro* angiogenesis model containing human umbilical vein endothelial cells (HUVEC's) expressing multiple fluorescent proteins. Sub-10-fs pulses can be propagated through polarization-maintaining single mode fiber (PMF) for use in NLOM. We demonstrate delivery of near transform-limited, 1 nJ pulses from a Ti:Al_2O_3 oscillator via PMF to the NLOM focal plane while maintaining 120 nm of bandwidth. Negative group delay dispersion (GDD) introduced to pre-compensate normal dispersion of the optical fiber and microscope optics ensured linear pulse propagation through the PMF. Nonlinear excitation of multiple fluorophores simultaneously and polarization

sensitive NLOM imaging using second harmonic generation in collagen was demonstrated using PMF delivered pulses. Two-photon excited fluorescence spectra and second harmonic images taken with and without the fiber indicates that the fiber based system is capable of generating optical signals that are within a factor of two to three of our traditional NLOM.

ACKNOWLEDGEMENTS

I would like to begin by extending my deepest respect and love to my wife, Christina, for all of her love, adoration and support throughout graduate school. She has unconditionally supported me in this endeavor and helped me to succeed to the highest levels of my ability. This is no small feat considering she is pursuing her own PhD in Clinical Psychology at the University of North Texas. Her persistence and personal drive, even in the face of adversity and difficult times, has always served as an inspiration.

I would also like to extend my love and gratitude to my parents, Leslie and Jeffrey if for no other reason than giving birth to and raising me; again, no small feat. Their careful nurturing provided the foundations on which I have built my personal, academic and finally professional careers. My brother Jason has always been there for me in any situation. He is quick to lend a helping hand or offer sage advice.

I would like to thank my advisor Prof. Alvin T. Yeh. He has provided guidance, knowledge, and allowed me to seek answers to many scientific questions. Prof. Kenith E. Meissner deserves credit on his open-door for technical discussions, curiosities or the department intramural soccer team. I extend thanks to my lab members, without whom, little of this work would be possible. They have assisted in the collection of data, provided numerous samples to image, and developed the control software for the microscope. In addition we have fostered a camaraderie that will not end with graduation.

Finally, I need to thank NuFern for providing some of the optical fibers used in this work and the Microscopy and Imaging Center at Texas A&M University for providing additional chirped mirrors.

TABLE OF CONTENTS

		Page
ABSTRACT.....		iii
ACKNOWLEDGEMENTS…….		v
TABLE OF CONTENTS…….		vi
LIST OF FIGURES…….		viii
LIST OF TABLES…….....		x
CHAPTER		
I	INTRODUCTION……	1
II	PRINCIPLES AND THEORY OF NONLINEAR OPTICAL MICROSCOPY……..	7
	2.1 Principles of Laser Operation……	7
	2.1.1 The Laser……	7
	2.1.2 Modelocking……...	11
	2.2 Nonlinear Optics……	14
	2.2.1 Self-Phase Modulation……	14
	2.2.2 Two-Photon Absorption…….	15
	2.2.3 Sum-Frequency Generation……	18
	2.3 Design of a Nonlinear Optical Microscope……...	22
III	CHARACTERIZATION OF SUB-10-FS PULSES……	31
	3.1 Dispersion and Ultrashort Pulse Measurement…….	31
	3.1.1 Dispersion……...	31
	3.1.2 Dispersion Compensation……...	34
	3.1.3 Ultrashort Pulse Measurement……	38
	3.2 Ex Vivo Characterization of Sub-10-fs Pulses……..	41
	3.3 Concluding Remarks……..	46
IV	MULTISPECTRAL NONLINEAR OPTICAL MICROSCOPY.	47
	4.1 Multispectral Nonlinear Optical Microscopic Imaging……..	47
	4.2 Characterization of Sub-10-fs Pulse Interactions with Common Dye Solutions..……	48

CHAPTER Page

4.3 Multispectral Imaging Using an *In Vitro* Angiogenesis Model…….. 51
4.4 Concluding Remarks…….. 55

V OPTICAL FIBER DELIVERY OF SUB-10-FS PULSES…… 57

5.1 Confinement of Light in Optical Waveguides…… 57
5.2 Optical Fiber Delivery of Ultrashort Pulses for Nonlinear Optical Microscopy…… 61
5.2.1 PMF Delivery of Femtosecond Pulses……. 64
5.2.2 Femtosecond Pulse Characterization for Nonlinear Optical Microscopy……. 66
5.3 Concluding Remarks…… 71

VI CONCLUSIONS AND FUTURE WORK…… 72

REFERENCES…….. 75

VITA…….. 85

LIST OF FIGURES

FIGURE		Page
2.1	Basic schematic of a laser.....	8
2.2	Quantum well diagram detailing the absorption of a photon from the pump laser promoting the Ti:Al_2O_3 electrons to the excited state.....	10
2.3	Soft aperture KLM…….	13
2.4	Quantum well diagram showing the simultaneous absorption of two long wavelength photons to satisfy the molecular transition to the excited state E_2^*……..	16
2.5	Spectrum of a sub-10-fs pulse…….....	17
2.6	Calculated T(ω) from the sub-10-fs laser spectrum, solid blue curve overlayed with the molecular two-photon excitation spectra of Indo-1 (cyan, diamonds), FITC (green, circles), TRITC (orange, triangles)....	18
2.7	Illustration of the simultaneous conversion of incident frequencies to the sum frequency……..	19
2.8	Scan waveforms for galvanometers……	23
2.9	Schematic of beam scanning for NLOM……	24
2.10	Schematic of a NLOM……...	27
2.11	Schematic of the coupling optics for the spectral detector……	30
3.1	Calculated dispersion curve of fused silica…….....	33
3.2	Schematic detailing the principles of a prism prechirper……...	37
3.3	Schematic of a chirped mirror stack……...	38
3.4	Schematic illustration of a second-order interferometric autocorrelator	40
3.5	Schematic diagram for ex-vivo pulse characterization……..	42
3.6	Interferometric autocorrelation at NLOM focal plane……...	45
4.1	10.4 fs autocorrelation of the pulse focused just within the cuvette…..	50
4.2	Absorption and emission spectra of three biological fluorophores….....	52
4.3	Emission spectra of three fluorescent probes…….	54
4.4	Emission spectra obtained from regions of interest within an image….	55
5.1	Refractive index profile of a single mode optical fiber……..	59

FIGURE Page

5.2 Plot of wavelength vs. *V*-number…… 59

5.3 Schematic representations of various polarization maintaining fiber designs……... 60

5.4 Basic schematic diagram for optical fiber delivery sub-10-fs pulses… 65

5.5 Pulse spectra normalized to energy directly from the oscillator (blue) and after propagation through PMF (red)…….. 66

5.6 Interferometric autocorrelation of fiber (A) and air (B) delivered pulses taken at the NLOM focal plane……... 67

5.7 Calculated T(ω) of the laser (blue) and PMF pulse spectra (red)…..... 69

5.8 Simultaneous excitation of Indo-1, FITC and TRITC using laser pulses delivered through air (blue) and PMF (red)…… 70

5.9 NLOM images of collagen fibers in rat skin using second harmonic generation with air (A) and fiber (B-C) delivered pulses……..... 71

LIST OF TABLES

TABLE		Page
3.1	Measured pulse parameters at the NLOM focal plane……	46
4.1	Emission, concentration, solvent and intensity slope of the dyes under test……	50

CHAPTER I
INTRODUCTION

Nonlinear optical microscopy (NLOM) utilizing femtosecond laser pulses has become a proven tool for intravital imaging of living tissues[1] since its first demonstration[2] nearly two decades ago. High peak intensities associated with femtosecond laser pulses focused through high numerical aperture (NA) objective lenses make nonlinear optical signals accessible from exogenous markers or endogenous biological constituents (e.g., two-photon excited fluorescence[3], TPEF, or second harmonic generation[4], SHG) with small nonlinear susceptibilities allowing for imaging and spectroscopy while minimizing sample damage via low average input powers. The nonlinear dependence of these optical signals on laser intensity facilitates optical sectioning, rendering thin images from within thick specimen, alleviating the need for destructive sample processing (i.e., fixing, sectioning, staining). These attributes are conducive for serial measurements that can follow the progression of biological processes in a single, living, experimental, thick tissue sample.

The high intensity laser pulses used in NLOM induce a polarization, P, that can be described as a Taylor expansion of the n^{th} order susceptibility of the sample, $\chi^{(n)}$, and the electric field, E,

$$P_i = \chi_{ij}^{(1)} E_j + \chi_{ijk}^{(2)} E_j E_k + \chi_{ijkl}^{(3)} E_j E_k E_l + \ldots \qquad (1.1)$$

Linear imaging techniques described by one-photon absorption (i.e. confocal fluorescence microscopy) and light scattering (i.e. confocal reflectance microscopy) are described by $\chi^{(1)}$. The remaining higher order terms fall under the realm of nonlinear microscopy. Traditionally, NLOM relies on second harmonic generation (SHG, a $\chi^{(2)}$ process) and two-photon excited fluorescence (TPEF, a $\chi^{(3)}$ process). Two-photon excitation is the simultaneous absorption of two photons whose summed energy satisfies

This dissertation follows the style and format of Optics Express.

a molecular two-photon transition. Second harmonic generation is the instantaneous annihilation of two photons and the creation of a single photon at half the wavelength. These processes will be investigated in further detail in chapter II. Other processes interrogated by NLOM include three-photon excitation, third harmonic generation, and Coherent Anti-Stokes Raman spectroscopy.

The optical signals generated in NLOM arise from the nonlinear interaction of NIR ultrashort (usually femtosecond pulses from a Ti:Al_2O_3 laser) pulses with the tissue of interest. Nonlinear interactions are characterized by the I^n (n indicating the order of the nonlinear process) dependence of signal on incident laser intensity (I_o). This nonlinear dependence on incident laser intensity confines signal generation to the region of highest photon density, the focal volume of the focusing objective lens. Elimination of fluorescence generated outside the focal plane reduces overall photodamage and oxidization.

The nonlinear processes governing signal generation in NLOM are maximized when pulse shape and duration at the sample are reconstructed. For a given average power, NLOM signals can be enhanced by increasing the peak power of the pulse. This is done by decreasing the repetition rate of the laser or by reducing the temporal duration of the pulse at the sample. The increase in peak power allows for increased depth penetration in highly scattering tissue samples[5-8]. Femtosecond optical pulses necessary to efficiently produce these signals are susceptible to phase distortions, i.e. dispersion, as pulses propagate through the optics of the imaging system[9], particularly as the temporal pulse duration decreases. Reduction in the temporal duration of laser pulses necessarily increases the spectral bandwidth associated with the pulse. Methods of pulse characterization will be discussed in chapter III.

The primary complication to *in-vivo* nonlinear multispectral imaging is the reliance on narrowband femtosecond laser pulses. Optimal fluorescence excitation efficiency necessitates the tuning of the laser to an absorption maximum for the individual contrast agents and rescanning of the tissue. The increased spectral bandwidth of temporally shorter pulses allows for the simultaneous excitation of multiple fluorophores without

the need for tuning. Broadband, sub-10-fs pulses, from our laser have a spectral bandwidth of ~125 nm FWHM. Two-photon excitation efficiency is determined by the overlap of the laser two-photon excitation power spectrum and the two-photon action cross section of the fluorescent probe of interest[1]. Sub-10-fs pulses, therefore, require careful control of the pulse duration at the sample which allows for all spectral components to contribue to fluorophore excitation. Furthermore, simultaneous excitation of multiple contrast agents greatly reduces the photo and thermal damage associated with rescanning the sample.

Optical molecular imaging is an emerging field comprising several complimentary techniques to provide information at the molecular, cellular, tissue, and whole-organism levels[10]. These techniques can be paired with emerging genomic and proteomic technologies[1, 11] enabling the development of fluorescent (protein) optical probes[12] and nanotechnologies allowing multifunctional imaging in real time with minimal or no invasion[13, 14]. Fluorescent proteins are increasingly being used to observe developmental events as they can be widely expressed in the cytoplasm or inserted into genes for specific cytogenetic profiling. Additional morphological and spectroscopic information can be obtained from the intrinsic contrast mechanisms available to NLOM. SHG requires highly ordered tissue structures, making it a constituent specific intrinsic contrast mechanism localized to collagen[15-17], cardiac myocites[18] and muscle sarcomeres[19]. Two-photon excited autofluorescence of NAD(P)H[20-26], flavoproteins[27], and mature elastin[28] provides morphological, spectroscopic and metabolic information surrounding cellular processes.

The minimally invasive nature of nonlinear microscopic imaging can provide concomitant morphological and chemo-physiological information within these tissues while following developmental progression or response to pathologic or mechanically induced stressors. Additionally, the wide range of detectable contrast mechanisms available to NLOM make it well suited to optical molecular imaging from the nano to macro scale. Therefore, efficient interpretation of these contrast mechanisms requires multispectral imaging capabilities. Multispectral imaging allows for the collection of an

entire spectrum for each individual pixel in an image. The presence and location of multiple constituent specific intrinsic and extrinsic contrast mechanisms can be observed simultaneously. For example, a collagen gel is seeded with cells expressing a particular fluorescent protein in its cytoplasm and two other fluorescent proteins transfected into adhesion molecules. Multispectral imaging allows morphological information comprising of the cytoplasmic fluorescent protein, extracellular matrix constituents, and the location of the adhesion molecules.

Further characterization of tissues in their native environment requires miniaturization of bench top microscopy systems into portable, optical fiber based imaging systems[29, 30]. The current state of technology surrounding NLOM limits the extent to which *in-vivo* experiments can be carried out. The specimen of interest must fit on the stage of an upright or inverted light microscope complicating the imaging of large, intact specimens. To this extent, the flexibility of NLOM systems is hindered by the need to orient the specimen to a fixed optical axis. Thus a flexible beam path allowed by fiber coupling the laser to the microscope will allow for the orientation of the imaging system to a region or specimen of interest. Optical fiber pulse delivery systems[31-34] provide a simple and efficient platform on which to develop miniaturized microscopes[35-37] and microendoscopes[29, 38-40] for tissue interrogation without excision. Fiber coupled imaging systems allow for the straightforward visualization of cells and extracellular matrix located within hollow tissue tracts and solid organs.

The benefits of optical fiber delivery of light from a remotely located source for cellular level imaging have been realized using confocal microscopy. Confocal microscopy is conducive to *in-vivo* imaging of superficial layers of skin[41, 42], eye[43], heart[44], gastrointestinal tract[45, 46], oral cavity[47, 48], nervous tissue[49] and the cervix[50]. The primary drawback to this technique is the use of excitation light in the blue region of the visible spectrum limiting overall imaging depth due to light scattering. Blue excitation light is necessitated by the use of autofluorescence or green emitting fluorescent probes (i.e. fluorescein) for signal generation and image formation.

Confocal reflectance techniques allow for the use of near infrared (NIR) light since the signal collected to render an image is derived from incident light being reflected back from the tissue. The second major drawback to confocal imaging techniques is the need for a confocal pinhole to reject out of focus light facilitating optical sectioning.

Despite the obvious advantage of NLOM over confocal microscopy techniques, it is relegated to use in academic research labs. Until recently, the femtosecond laser sources required for NLOM have been large and require well trained personnel to operate and maintain. Presently, there are several one box, turn-key, computer controlled femtosecond laser systems that allow for mode-locking and tuning to be accomplished with the push of a button. The second difficulty in making NLOM imaging systems compatible with large tissue (and whole-animal) studies are the inherent challenges associated with coupling high intensity femtosecond pulses into optical fiber. The susceptibility of ~100 fs pulses to severe nonlinear broadening, a phenomenon associated with the interaction of intense pulses with the glass core of an optical fiber discussed in chapter IV, limits power delivered to the specimen or requires complex optical systems to control. Nonlinear broadening makes the preservation of temporal and spectral characteristics of ~100 femtosecond laser pulses at the focal plane using traditional step-index single mode optical fibers challenging.

A new class of optical fiber has been developed which permit the propagation of intense ultrashort pulses without the detrimental effects of nonlinear broadening. Hollow core photonic crystal fibers[51] (HC-PCF's), as their name suggests, have a periodic array of holes forming a 2D crystal lattice comprising the cladding surrounding a central defect in the crystalline structure as the core. This periodic crystalline structure confines frequencies whose propagation vectors are forbidden from traveling through the structure to the core. The corresponding air core has a very high threshold for nonlinearity compared to the glass of step-index fibers allowing for the undistorted propagation of intense pulses[52]. The photonic crystal structure of the cladding allows core geometries to be created that are impossible with the total internal reflection mechanism of confinement required by step-index optical fiber.

This dissertation will detail the principles of NLOM, femtosecond pulse characterization, multispectral imaging, and optical fiber delivery of sub-10-fs pulses. Principles of mode-locked laser operation and nonlinear optics will also be discussed as they pertain to NLOM. The research covered within this document serves as a basis for developing a freely translatable NLOM that can be oriented to a region of interest on a large (e.g. whole animal) specimen.

CHAPTER II
PRINCIPLES AND THEORY OF NONLINEAR OPTICAL MICROSCOPY

NLOM is a laser scanning imaging technique that typically relies on femtosecond pulsed lasers to generate observable signals through nonlinear interactions with the tissue. Sec. 2.1 discusses the principles of laser operation and mode-locking as they pertain to the Ti:Al_2O_3 laser. Although other types of lasers have been used[53] in NLOM, they will not be discussed here. Sec. 2.2 focuses on the nonlinear interactions governing two-photon absorption and second harmonic generation. Finally, Sec. 2.3 discusses system design in NLOM.

2.1 PRINCIPLES OF LASER OPERATION

2.1.1 The Laser

The critical element to all lasers, the gain medium, is a material capable of amplifying radiation. Stimulated emission, the principle responsible for amplification was first discovered in 1916 by Albert Einstein, though the first laser was not constructed until 1960 by T. H. Maiman. Briefly, as illustrated in Fig. 2.1, energy is imparted onto the gain medium by an external source. The gain medium is encased in a highly reflective cavity that contains the amplified light and redirects it back through the gain medium for further amplification. A method to extract the light from the cavity must be implemented, and is typically a reduction in reflectivity at one end of the cavity.

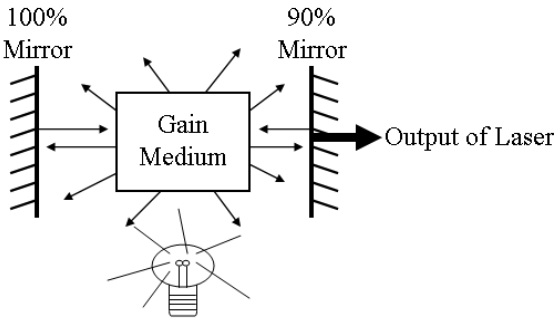

Fig. 2.1. Basic schematic of a laser.

In order for stimulated emission to take place photons equal to the relaxation energy of the gain medium must be present. These photons arise from the absorption of pump energy by the gain medium and the resulting spontaneous emission of light as electrons undergo relaxation to the ground state. Pump energy can be imparted optically by another laser or intense light source or electrically by passing a current through the gain medium. Our discussion will focus on optical pumping by another laser as is standard with Ti:Al_2O_3 oscillators.

A laser, either an Agron ion or more commonly frequency double Nd:YVO_4, is focused onto the Ti:Al_2O_3 crystal. The absorption of green light from the pump laser promotes the Ti:Al_2O_3 to an excited state. The radiative relaxation, spontaneous emission, from the excited state emits a photon of lower energy than the pump light, in this case around 800nm and is illustrated in Fig. 2.2. The bandwidth of the spontaneous emission determines the gain width of the laser. Stimulated emission occurs when one of these photons collides with an electron in the excited state causing it to rapidly fall to the ground state and emit a second photon creating the process of amplification. Under ordinary circumstances stimulated emission would rapidly deplete the excited state and amplification would cease. To counteract this, a population inversion, where more electrons are in the excited state than ground state, is required. The population of electrons for a basic two-level system in the ground (N_1) and excited states (N_2) is described by the following rate equations[54]

$$\dot{N}_1 = -\Gamma_1 N_1 + A_{21} N_2 + \sigma\Phi\left(N_2 - N_1\right) \tag{2.1a}$$

$$\dot{N}_2 = -\Gamma_2 N_2 - A_{21} N_2 - \sigma\Phi\left(N_2 - N_1\right) \tag{2.1b}$$

where Γ is the elastic collision rate, N is the population density, A_{21} is the spontaneous emission rate, σ is the atomic absorption cross section and Φ is the incident photon flux. By adding these two equations together, it can be seen that eventually elastic collisions will deplete both states. The magnitude of Γ is small relative to A_{21} and σΦ and can be ignored under most intermediate time conditions. This then leaves

$$\dot{N}_1 = A_{21} N_2 + \sigma\Phi\left(N_2 - N_1\right) \tag{2.2a}$$

$$\dot{N}_2 = -A_{21} N_2 - \sigma\Phi\left(N_2 - N_1\right) \tag{2.2b}$$

and after again summing 2.2a and 2.2b we can see that $\dot{N}_1 + \dot{N}_2 = 0$ which means that with no inelastic collisions $N_1 + N_2 = N = \text{constant}$. We can now rewrite the rate equation using only N_2

$$\dot{N}_2 = -A_{21} N_2 - \sigma\Phi\left(2N_2 - N\right) = -\left(A_{21} + 2\sigma\Phi\right) N_2 + \sigma\Phi N \tag{2.3}$$

which has the solution under constant pumping

$$N_2(t) = \left[N_2(0) - \frac{N\sigma\Phi}{A_{21} + 2\sigma\Phi} \right] e^{-\left(A_{21} + 2\sigma\Phi\right)t} + \frac{N\sigma\Phi}{A_{21} + 2\sigma\Phi} \tag{2.4}$$

Under the conditions of intense pumping ($\sigma\Phi >> A_{21}$) we can see that a saturated excited state can only contain half the population. Under these intense steady-state conditions power-broadening of the Lorentzian line function of the excited state allows for a population inversion.

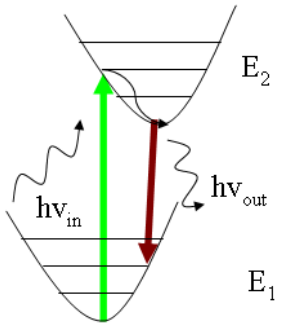

Fig. 2.2. Quantum well diagram detailing the absorption of a photon from the pump laser promoting the Ti:Al_2O_3 electrons to the excited state. The electron relaxed spontaneously back to the ground state emitting a photon.

Following the establishment of a population inversion, stimulated emission will dominate over absorption and amplification of the radiation within the cavity begins to occur. The frequencies at which gain occurs are determined by the longitudinal cavity modes of the laser. In order to satisfy the cavity resonance condition, the end mirrors must be separated by an integer number of half wavelengths ensuring that the electric field vanishes at the walls of the cavity. The resonant frequency is given as

$$\upsilon = \frac{nc}{2L} \tag{2.5}$$

where n is an integer and L is the cavity length. Practically speaking, for visible and near-infrared wavelengths the cavity length is many times longer than the wavelength of amplified light allowing many cavity modes to exist simultaneously. The spacing between cavity modes is then obviously

$$\Delta\upsilon = \frac{c}{2L} \tag{2.6}$$

and the number of supported cavity modes is the gain width divided by Equation 2.6. Amplification of resonant frequencies within the cavity gives laser radiation its coherent properties.

We have now established to conditions under which lasing can occur. In order to achieve lasing amplification must overcome the cavity losses imposed by scattering, absorption, and output loss. Output loss is the portion of the laser lost through the output

coupler as the laser beam. The amount of gain necessary to equal these losses is the threshold condition for laser oscillation. The gain threshold is then given as

$$g_t = -\frac{1}{2l}\ln(r_1 r_2) + a \qquad (2.7)$$

where r_1 and r_2 are the end mirror reflectivities, l is the gain medium length and a is the additional cavity loss. Cavity modes that exceed this condition will lase.

2.1.2 Modelocking

Lasing cavity modes are used to generate pulses from the cavity. The time duration of a laser pulse is the Fourier transform of the spectral content of the pulse. Meaning, the more cavity modes that can be used to generate a pulse, the shorter its duration becomes. Theoretically, the shortest possible pulse a laser can produce is proportional to the inverse of the laser gain width. For short pulse generation and modelocking the phases of each of the lasing cavity modes are locked. The superposition of cavity modes through constructive interference generates the intensity of the pulse. Destructive interference between cavity modes away from the phase locked peak suppresses the energy creating the pulse train. The locked phases of the cavity modes dictates that the duration between pulses equals the roundtrip time within the cavity. Most short pulse lasers rely on passive modelocking using a saturable absorber, semiconductor saturable absorber (SESAM) or Kerr lens modelocking (KLM). Passive methods of modelocking are capable of generating sub-100-fs pulses directly from a laser oscillator. The shortest pulse achieved to date directly from a Ti:Al_2O_3 oscillator is <6fs[55-57]. Active modelocking involves the use of electro optic components, predominantly acousto-optic modulators for acoustic loss modulation or pockels cells in electro-optical phase modulation. Active modelocking is generally not used for ultrashort pulse generation due to its complexity to implement.

To generate pulses with a larger spectral extent than the gain medium directly from the laser oscillator without external compression, nonlinear interactions within the laser crystal must be exploited. In our laser, modelocking through the optical Kerr effect and self-phase modulation (SPM, Sec 2.2.1) is used to generate sub-10-fs pulses. The Kerr

effect, intensity dependent refractive index of a medium, causes the refractive index of the gain medium to be altered as

$$n(t) = n_0 + n_2 I(t) \tag{2.8}$$

where *I(t)* is the time dependent laser intensity and n_2 is the material dependent nonlinear portion of the refractive index. This effectively produces a gradient index lens within the gain medium. The buildup of cavity intensity causes the laser beam to self-focus following the intensity gradient profile. This self focusing creates a pulsed beam of narrower diameter relative to the continuous wave (CW) beam. In hard aperture KLM a pinhole or slit is used to block, i.e. induce loss, the larger diameter CW beam. Soft aperture, or gain aperture, KLM induces loss in the CW beam by detuning a focusing mirror relative to the gain medium and second focusing mirror in a near confocal resonator cavity. The pulsed beam has a smaller diameter than the CW beam allowing for better overlap of the tightly focused pump and the pulsed beam. This increases the gain efficiency for the pulsed beam when the resonator is in stable operation. Mirror tuning range is dependent on the focusing parameters of the curved mirrors and their confocal parameters[58-60]. The drawback to KLM is a decrease in long term laser stability as the resonator must be operated near the edge of stability to favor modelocking. A schematic of a KLM oscillator is depicted in Fig. 2.3. Although this arrangement is not self-starting, modelocking can robustly be induced by toggling an end mirror.

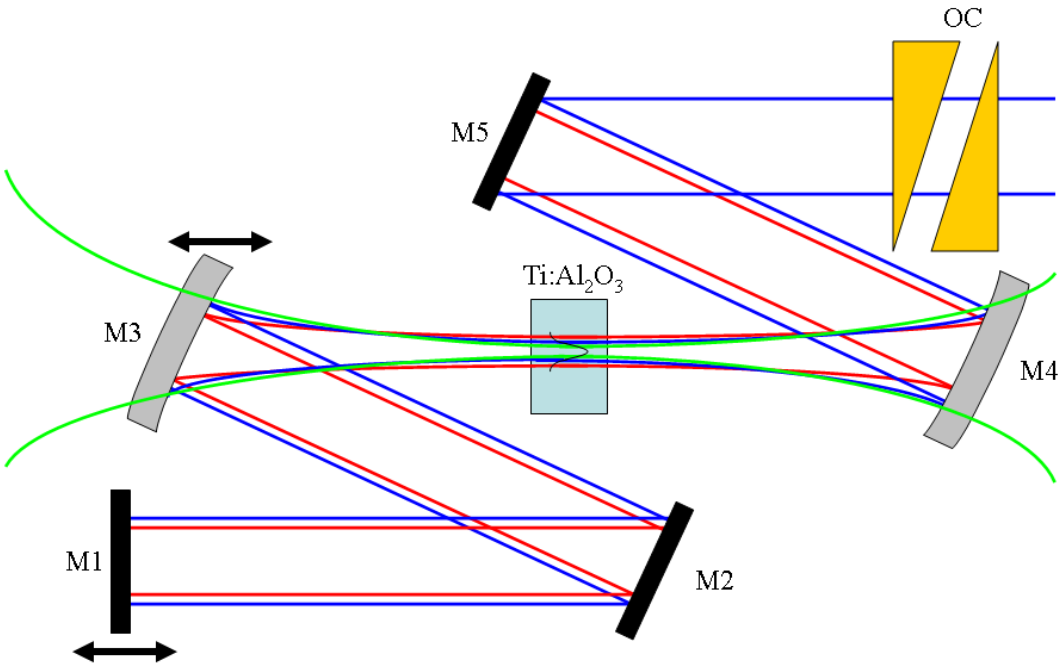

Fig. 2.3. Soft aperture KLM. The Gaussian curve in the gain medium indicates the intensity dependent refractive index profile induced by the optical Kerr effect. The double headed arrow above M3 indicates the detuning of the curved mirror to favor CW or pulsed operation. Toggling of M1 will induce modelocking. Green: Pump beam. Red: CW beam. Blue: Pulsed beam. M1: End mirror. M2 & M5: Intracavity mirrors. M3 & M4: Curved mirrors. OC: Output coupler.

The second consequence of the optical Kerr effect is SPM. SPM results in the spectral broadening of the pulse allowing KLM laser to obtain pulse bandwidths wider than the gain width. For this to occur efficiently the positive frequency chirp induced by SPM must be counteracted with negative intracavity group-velocity dispersion (GVD, Sec. 3.1). This balance of SPM induced chirp and negative intracavity dispersion allows the formation of soliton-like pulses propagating with an invariant shape and inherently locked phases necessary for modelocking. The advantage of soliton-like pulse propagation through the laser cavity comes from their intrinsic stability and naturally occurring $sech^2$ pulse shape. For pulses of ultrashort duration, i.e. sub-10-fs, the dispersion compensation must include higher order terms to maintain stability and to obtain ultrashort pulses directly from the oscillator. It should be noted

that our laser does require external dispersion compensation to account for the output coupler only.

The superposition of cavity modes to generate ultrashort pulses is directly responsible for the high instantaneous intensity. A pulse essentially contains all the energy that would exist in a continuous wave beam into discrete packets. Pulse energy is then defined as the average laser power divided by the repetition rate. The peak power of a *sech*^{2} pulse is therefore

$$P = .88\left(\frac{E_p}{\tau_o}\right) \tag{2.9}$$

where E_p is the pulse energy, τ_o is the Full-Width-Half-Maximum (FWHM) pulse duration and the .88 is a deconvolution factor.

2.2 NONLINEAR OPTICS

2.2.1 Self-Phase Modulation

We have already seen that the optical Kerr effect induces an intensity dependence to the refractive index. From the nonlinear polarization, Equation 1.1, induced by the applied field the linear refractive index is described under the $\chi^{(1)}$ terms and the nonlinear refractive index falls under $\chi^{(3)}$ terms. SPM is the phase change of an optical pulse resulting from the nonlinearity of the refractive index. Assuming a sech^2 pulse of the form

$$I(t) = I_o \operatorname{sec}\mathrm{h}^2\left(\frac{\tau}{\tau_o}\right) \tag{2.10}$$

The phase change associated with this profile described by Equation. 2.8 is

$$\phi_{NL}(t) = -n_2\frac{\omega_o}{c}LI(t) = -n_2\frac{\omega_o}{c}LI_o \operatorname{sec}\mathrm{h}^2\left(\frac{\tau}{\tau_o}\right) \tag{2.11}$$

where L is the propagation length through the medium, ω_o is the center frequency, and c is the speed of light. We can rewrite Equation 2.11 in terms of the peak power of the pulse

$$\phi_{NL} = \gamma P_o = \frac{2n_2\omega_o L}{c\pi w^2} P_o \qquad (2.12)$$

where γ is the nonlinearity coefficient, P_o is the pulse peak power, and w is the $1/e^2$ radius of the Gaussian beam. The phase change causes the pulse to undergo an instantaneous frequency shift

$$\delta\omega = -\frac{d\phi_{NL}(t)}{dt} = \frac{2\omega_o}{c} L n_2 \frac{dI(t)}{dt} = \frac{2\omega_o}{c\tau_o} L n_2 I_o \operatorname{sec h}^2\left(\frac{\tau}{\tau_o}\right)\tanh\left(\frac{\tau}{\tau_o}\right) \qquad (2.13)$$

This instantaneous frequency shift, assuming n_2 is positive from normal dispersion (Sec. 3.1), will cause the leading edge of the pulse to be shifted to lower frequencies and the trailing edge to higher frequencies[61]. In the event of anomalous dispersion SPM will cause frequencies to be shifted in the opposite manner leading to spectral narrowing. Linear chirp associated with the instantaneous frequency shift is

$$\alpha = \frac{2\omega_o}{c\tau_o} L n_2 I_o \qquad (2.14)$$

As stated earlier, soliton formation is the result of an exact compensation of linear chirp due to SPM and negative GVD. Satisfying these conditions creates a fundamental soliton that is shape invariant. Increasing the intensity creates higher order solitons whose shape changes with propagation distance in a periodic manner. The propagation distance required for the pulse shape to be reconstructed is the soliton period.

2.2.2 Two-Photon Absorption

Two-photon absorption (TPA) was first predicted in 1931 by Maria Göppert-Mayer[62]. It was not, however, until the invention of the laser that it was observed in inorganic crystals[63]. TPA in organic crystals[64] and then in dilute organic solution[65] was first reported in 1963 using a pulsed Ruby laser. The first demonstration of TPA in fluorescent biological samples was not demonstrated until 1990[2].

In the previous section we described fluorescence in terms of spontaneous emission as the radiative decay of a molecule from an excited state back to the ground state. For the purposes of our laser, only one photon is required to satisfy the allowed energy

transition (resonant interaction) between the ground state and the excited state. Multiphoton absorption, the simultaneous absorption of multiple photons to satisfy an allowed energy transition mediated through a virtual transition state, is a resonant interaction related to an odd-power nonlinear susceptibility depicted in Fig. 2.4. Since the process requires two photons to arrive at the absorbing medium simultaneously and in phase, the high intensity of femtosecond pulses is required to maintain reasonable average power for survival of live biological specimen[66-69]. We can describe the probability of a two-photon transition as

$$V_{il} \approx \sum_{l} \left[\frac{\left\langle f \left| \hat{\varepsilon}_1 \bullet \rho \right| l \right\rangle \left\langle l \left| \hat{\varepsilon}_2 \bullet \rho \right| i \right\rangle}{E_l - E_i - \hbar\omega_2} + \frac{\left\langle f \left| \hat{\varepsilon}_2 \bullet \rho \right| l \right\rangle \left\langle l \left| \hat{\varepsilon}_1 \bullet \rho \right| i \right\rangle}{E_l - E_i - \hbar\omega_1} \right]^2 \qquad (2.15)$$

where f is the final excited state, i is the initial ground state, l is the virtual intermediate state, $\varepsilon \bullet \rho$ describes the density of states and ω are the frequencies of the incident photons. It should be noted that for TPA the frequencies need not be identical since the absorption probability is summed across all intermediate states. Virtual states only exist when a pulse is present. Therefore, a more accurate representation, using the bandwidth of a sub-10-fs pulse for reference, is shown in Fig. 2.5.

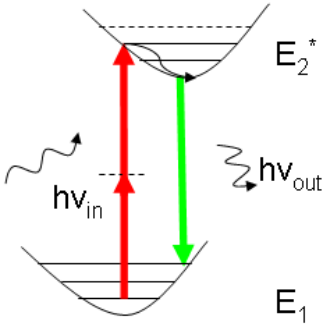

Fig. 2.4. Quantum well diagram showing the simultaneous absorption of two long wavelength photons to satisfy the molecular transition to the excited state E_2^*. The dashed line represents the virtual intermediate state.

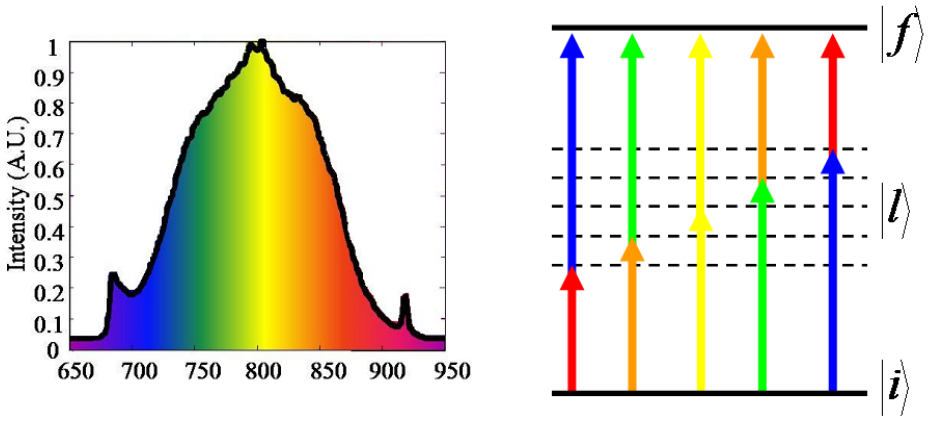

Fig. 2.5. Spectrum of a sub-10-fs pulse. Rainbow coloring is added for reference to colored arrows. Jablonski diagram showing absorption of any frequency combination from the incident pulse to satisfy the molecular transition from *i* to *f*.

Equation 2.15 indicates that for a uniformly absorbing medium all frequency components will contribute to the excitation provided they arrive in phase and motivates the use of ultrashort pulses for TPA in NLOM. Therefore, since pulse spectral content and pulse duration are inversely proportional one would expect the increase in fluorescence to scale as $1/\tau_o$. Fluorescent contrast mechanisms, however, do not have uniform absorption cross sections which imposes a physical limit on the $1/\tau_o$ scaling of fluorescence to pulse width. This is of particular importance when using sub-10-fs pulses with a bandwidth >125nm. The transition rate for TPA can then be described as

$$R_{fi}^{(2)} = \sigma_{fi}^{(2)}(\omega) I^2 \qquad (2.16)$$

where $\sigma^{(2)}(\omega)$ is the two-photon molecular absorption profile. Non-resonant two-photon excitation by femtosecond pulses can be understood by examining the two-photon excitation power spectrum[70, 71],

$$T(\omega) = \left| \int_0^\infty E\left(\omega/2 + \Omega\right) E\left(\omega/2 - \Omega\right) d\Omega \right|^2 \qquad (2.17)$$

where $E(\omega)$ is the Fourier transform of electric field $E(t)$ and Ω is an iterative variable that ensures integration over non-degenerate (sum frequency) and degenerate (second

harmonic) frequency combinations. The probability of non-resonant two-photon absorption is proportional to the overlap integral[72, 73],

$$\Gamma \propto \int_{-\infty}^{\infty} \sigma^{(2)}(\omega) T(\omega) d\omega \qquad (2.18)$$

where $\sigma^{(2)}(\omega)$ is the molecular two-photon absorption spectra. Assuming transform limited pulses, calculated $T(\omega)$ calculated from the sub-10-fs laser spectrum is overlayed with the molecular two-photon absorption spectra of three common biologically relevant fluorophores in Fig. 2.6. It should be noted that since one-photon absorption follows odd-parity selection rules and TPA follows even-parity selection rules (meaning one-photon absorption and TPA do not excite to the same state) one should not expect the two-photon molecular absorption spectra to be twice the wavelength of the one-photon absorption for symmetric molecules.

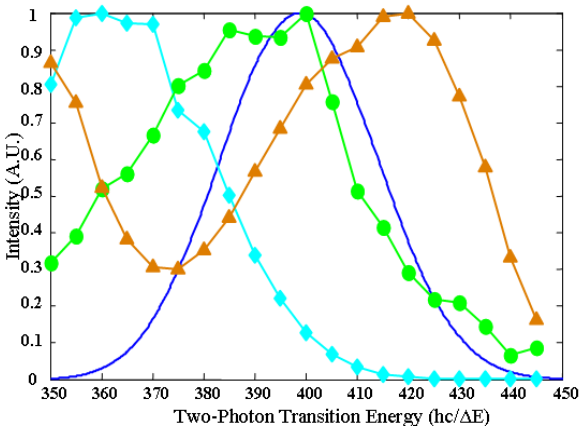

Fig. 2.6. Calculated T(ω) from the sub-10-fs laser spectrum, solid blue curve overlayed with the molecular two-photon excitation spectra of Indo-1 (cyan, diamonds), FITC (green, circles), TRITC (orange, triangles).

2.2.3 Sum-Frequency Generation

Sum-frequency generation (SFG) is a coherent second order nonlinear process that follows $\chi^{(2)}$ susceptibility. Being an even-order process, there is a quantum mechanical requirement of a lack of inversion symmetry to produce SFG. SFG is a coherent process

and therefore, does not involve the absorption of two long wavelength photons followed by the emission of a single short wavelength photon. Rather, SFG is the simultaneous annihilation of two low frequency photons and creation of a single high frequency photon at the sum of the two incident frequencies. Second harmonic generation (SHG) is a degenerate case of SFG where the two incident photons have identical frequencies illustrated in Fig. 2.7. Owing to the narrow bandwidth of most ~100fs lasers typically used in NLOM, SHG is a reasonable approximation of the signal generation method. As examined previously with TPA and assuming a uniform conversion efficiency of the crystal, complete phase matching across the spectrum and a transform limited pulse, the "SHG" signal generated from sub-10-fs pulses will be proportional to T(ω) from Equation 2.17.

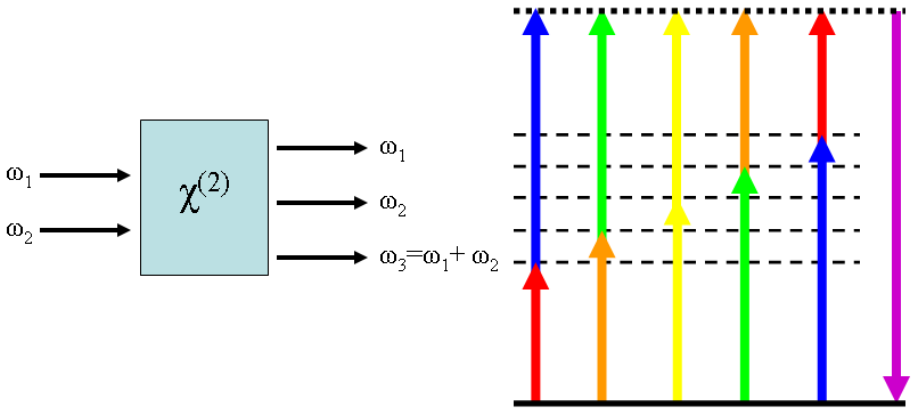

Fig. 2.7. Illustration of the simultaneous conversion of incident frequencies to the sum frequency. The dashed line of the "excited" state indicates this is not a resonance excitation. The degenerate case where $\omega_1=\omega_2$ for SHG is shown by the yellow arrows.

SFG is a three wave mixing process we define a plane wave for each frequency of the field

$$E_1(z,t) = A_1 e^{i(k_1 z-\omega_1 t)} + C.C. \qquad (2.19a)$$

$$E_2(z,t) = A_2 e^{i(k_2 z-\omega_2 t)} + C.C. \qquad (2.19b)$$

$$E_3(z,t) = A_3 e^{i(k_3 z-\omega_3 t)} + C.C. \qquad (2.19c)$$

where $k_n = \frac{n\omega_n}{c}$, A_n is the electric field amplitude and assumed to be constant; we introduce the wave equation

$$\nabla^2 E_n - \frac{\varepsilon^{(1)}(\omega_n)}{c^2}\frac{\partial^2 E_n}{\partial t^2} = \frac{1}{\varepsilon_o c^2}\frac{\partial^2 P_n^{NL}}{\partial t^2} \tag{2.20}$$

From the right hand side of Equation 2.20 we can see that there is a nonlinear source term corresponding to ω_3 stemming from the nonlinear polarization in Equation 1.1 defined as

$$P_3(z,t) = P_3 e^{i\omega_3 t} + C.C. \tag{2.21}$$

and the amplitude P_3 is defined as

$$P_3 = 4\varepsilon_o d_{eff} A_1 A_2 e^{i(k_1+k_2)z} \tag{2.22}$$

where d_{eff} is determined from the second order-nonlinear susceptibility tensor matrix derived from the crystal structure. It can be seen that the amplitude of the nonlinear source term is dependent on the intensity of the driving fields and their corresponding wavevectors. We have presented all of the terms that make up the wave equation (Equation 2.20) by plugging in Equations 2.19c, 2.21 and 2.22 we obtain

$$\frac{d^2 A_3}{dz^2} + 2ik_3\frac{dA_3}{dz} = \frac{-4d_{eff}\omega_3^2}{c^2} A_1 A_2 e^{i(k_1+k_2-k_3)z} \tag{2.23}$$

Assuming the slowly varying amplitude condition, the fractional change in the amplitude in a distance on the order of wavelength is small, we can neglect the first term on the left hand side of the equation as it is much smaller than the second term and write coupled wave equations for all three frequencies. They are termed coupled wave equations because the electric field for each frequency is dependent on the electric field of the other two frequencies.

$$\frac{dA_1}{dz} = \frac{2id_{eff}\omega_1^2}{k_1 c^2} A_3 A_2 e^{i\Delta kz} \tag{2.24a}$$

$$\frac{dA_2}{dz} = \frac{2id_{eff}\omega_2^2}{k_2 c^2} A_3 A_1 e^{i\Delta kz} \tag{2.24b}$$

$$\frac{dA_3}{dz} = \frac{2id_{eff}\omega_3^2}{k_3 c^2} A_1 A_2 e^{i\Delta kz} \tag{2.24c}$$

We have introduced a new term Δk, the wavevector mismatch

$$\Delta k = k_1 + k_2 - k_3 \tag{2.25}$$

which is the degree of dephasing of the generated wave with respect to the nonlinear polarization. Therefore, under perfect phase matched conditions each atomic dipole in the crystal emits a field in phase allowing for the coherent superposition of all atomic dipoles following the propagation vector, i.e. in the forward direction. It is then convenient for microscopy to express the sum-frequency in terms of intensity by integrating Equation 2.24c over the interaction length of the nonlinear medium as

$$I_3 = \frac{8n_3\varepsilon_o d_{eff}^2 \omega_3^4 |A_1|^2 |A_2|^2}{k_3^2 c^3} \left| \frac{e^{i\Delta kL} - 1}{\Delta k} \right|^2 \tag{2.26}$$

and substituting intensity for field amplitude Equation 2.26 becomes

$$I_3 = \frac{8d_{eff}^2 \omega_3^2 I_1 I_2}{n_1 n_2 n_3 \varepsilon_o c^2} \left| \frac{e^{i\Delta kL} - 1}{\Delta k} \right|^2 \tag{2.27}$$

Equation 2.27 indicates the intensity of the sum-frequency scales with the square of the electric field as expected for a second order process. The wavevector mismatch is only present in the squared modulus on the right hand side of the equation. Multiplying this term out and applying the appropriate trigonometric identity, the modulus takes the form

$$\left| \frac{e^{i\Delta kL} - 1}{\Delta k} \right|^2 = L^2 \sin c^2 \left(\frac{\Delta kL}{2} \right) \tag{2.28}$$

From this we can see that the large wavevector mismatch associated with the broad spectral extent of sub-10-fs pulses propagating through a nonlinear medium will rapidly diminish the intensity of the signal. Fortunately interaction length in highly ordered crystalline structures in biology (i.e. collagen fibers) is on the order of 1μm allowing large Δk to be tolerated and matching the focal volume of high NA objective lenses.

It is also possible for SFG (and thusly SHG) to be generated at an interface of a linear and nonlinear medium in the backward direction. This seems contradictory to the

coherent nature, and forward propagation of the sum-frequency signal. Conservation of energy and Fresnel reflection indicate that a small portion of the sum-frequency signal should be reflected[61, 74]. The short interaction holds further advantages in the realm of NLOM allowing backward propagating SFG to be detected by the focusing objective since each fibril becomes its own nonlinear medium. In this case the short interaction length of the collagen fiber cross section and focused beam dictates that the backscattered and forward propagating signals are similar. From this relation it is possible to determine the size of a collagen fibril as a function of forward to backward propagating second harmonic[16]. Larger fibrils will have a greater intensity in the forward direction.

2.3 DESIGN OF A NONLINEAR OPTICAL MICROSCOPE

The previous section detailed the two most common nonlinear optical processes used to generate signal in NLOM. In this section we will detail the optical considerations in designing a NLOM. The nonlinear dependence of the optical signals detected confines their origin to the region of highest intensity, the focal volume of the objective lens only. This creates optically thin images containing axial information on the order of a micron. Optical signals are then detected by a photomultiplier tube (PMT) or a CCD. The output of the detector is then read by a computer which renders an image based on detector signal vs. scanner position. We will discuss beam scanning, image generation, excitation and detection optics as they pertain to the system developed in our laboratory.

NLOM is a point laser scanning microscopy technique. Images are rendered by scanning (typically in a saw-tooth or triangle pattern) a laser beam focused to a diffraction limited spot across a specimen to render an *en-face* image. Traditionally, galvonometrically driven mirrors are used for beam scanning, however, resonance scanners[75] and acousto-optic modulators[76] have been used for high speed applications. In galvanometer scanning systems the x-axis scans at high speed creating a line scan. Two dimensional scanning is accomplished with a second y-axis mirror

scanning very slowly relative to the x-axis where one frame represents the total scan angle of the y-axis. This is schematically depicted in Fig. 2.8.

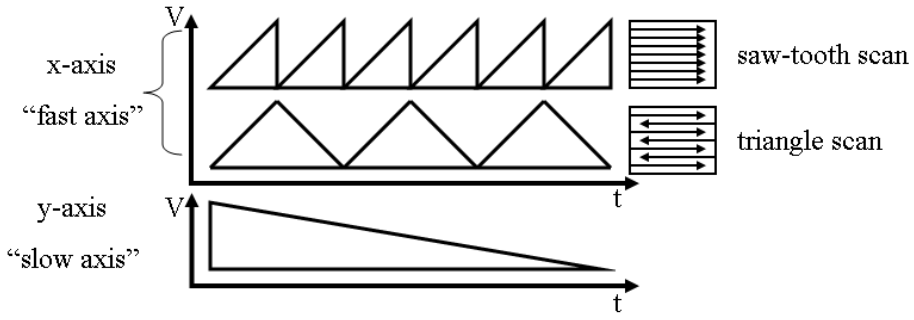

Fig. 2.8. Scan waveforms for galvanometers.

To translate the scanning beam to the specimen plane the scan mirrors must be appropriately imaged onto the back focal aperture (BFA) of the objective lens. Keplerian telescopes are traditionally used with a point between the scan mirrors placed one focal length from the first lens in the telescope. The BFA is located one focal length away from the second lens in the telescope with the two lenses separated by the sum of their focal lengths. In this arrangement the scanning mirrors create a pivot point at the BFA where the beam is stationary in a 2D plane and the scan mirrors and BFA are in conjugate planes. The second advantage in using this telescope allows the beam to be expanded to fill the BFA using appropriate selected focal length lenses. The magnification of the telescope is given as the ratio of focal lengths $M = \frac{f_2}{f_1}$. The beam scanning optics for NLOM are schematically presented in Fig. 2.9.

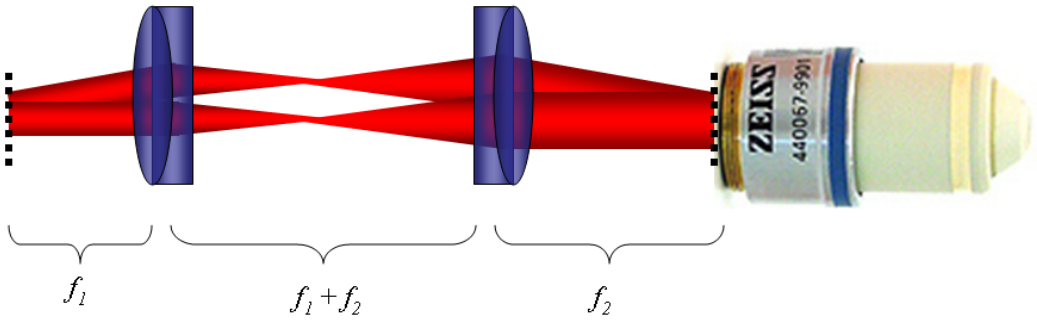

Fig. 2.9. Schematic of the beam scanning for NLOM. The dashed lines represent the conjugate planes of the scan mirrors and BFA.

Since we are scanning a single point and detecting the signal on a "single pixel" detector (image pixel intensity is determined by overall detector output regardless of the number of channels the detector contains) image resolution is solely determined by the imaging optics and typically defined by the Rayleigh criterion. The Rayleigh criterion indicates that two points of equal intensity are said to be resolved the principle maximum of one point falls on the first minimum of the second point. The intensity distribution of the radial focal field for a plane wave focused to a diffraction limited point is given by

$$I(0,v) \propto \left| \frac{2J_1(v)}{v} \right|^2 \tag{2.29}$$

where $J_1(v)$ is a first order Bessel function of the first kind and

$$v = r\frac{2\pi}{\lambda}\sin\alpha \tag{2.30}$$

with r being the radial coordinate and α being the half angle of the focused beam. Therefore, the lateral resolution of the system is

$$r_o = \frac{.61\lambda}{NA} \tag{2.31}$$

In the axial direction, the intensity distribution is described by a sinc^2 function, yielding a broader axial distribution. Axial resolution is definied as

$$z_o = \frac{2n\lambda}{NA^2} \tag{2.32}$$

These resolution numbers are slightly misleading as they do not take into account that nonlinear interactions are confined to within the focal volume. This leads to an improvement in both axial and lateral resolution where[3]

$$r_o = \frac{.32\lambda}{\sqrt{2}NA}(NA \le 0.7) \tag{2.33a}$$

$$r_o = \frac{.325\lambda}{\sqrt{2}NA^{.91}}(NA \ge 0.7) \tag{2.33b}$$

$$z_o = \frac{.532\lambda}{\sqrt{2}}\left[\frac{1}{n-\sqrt{n^2-NA^2}}\right] \tag{2.34}$$

After taking into account the resolution improvements afforded by the nonlinear interaction volume, NLOM have similar, though still lower, resolution than traditional one-photon microscopy techniques.

NLOM detection optics can be configured in a back-reflected (focusing objective collects optical signals), transmission (opposing objective or condenser lens collects optical signals) or a combination of the two. Detection geometry is determined by the experimental conditions. Imaging of thick biological tissues generally requires a back-reflected setup and will be considered here. Transmission geometries are often reserved for transparent or thin tissues.

Optical signals generated within the tissue are collected by the focusing objective. Collection efficiency of these signals is a function of the NA of the objective. Higher NA will allow the objective lens to collect photons that have been emitted or scattered at higher angles from the tissue. It should be noted that higher NA lenses do not always produce the brightest images as the front lens becomes small. Long working distance objectives offer a good compromise between NA (and hence resolution) and front lens diameter while allowing for deep tissue imaging.

In NLOM signal collected by the objective lens can immediately be focused onto a detector. Unlike traditional light microscopy where image forming optics are necessary to view the sample in an image plane, the point by point stitching of NLOM images allows the detector to be placed anywhere in the optical path. Losses in the microscope

can be eliminated by placing the detector directly behind the objective lens. Unfortunately, most NLOM systems are converted from upright or inverted microscopes and placement of the detector immediately behind the objective is inconvenient. In our system the detectors are located at the top port of the trinocular head.

Backscattered light from the tissue is composed of back-scattered laser light and the spectral constituents of the contrast mechanisms (i.e. fluorescence or SHG) in the tissue. Enhancement of contrast in NLOM images requires the appropriate splitting of these signals from each other. A primary dichroic mirror (a mirror that is designed to reflect and transmit a specific set of wavelengths) is inserted into the beam path allowing the excitation optics and detection optics to share a single common element, the objective. Light collected by the objective is passed through the primary dichroic mirror where much of the backscattered laser light is reflected out of the beam. Segmentation of the collected signal light is accomplished by a set of secondary dichroic mirrors that reflect light below a desired cutoff wavelength that corresponds to the contrast mechanism of interest. Bandpass filters are placed after the secondary dichroic to further eliminate backscattered laser light and to place tighter wavelength restrictions on the signal read by the detector. This allows individual detectors to read signal originating from a particular contrast mechanism. The image channels can be recombined in post processing to form a complete image. Fig. 2.10 illustrates the full optical path of an NLOM from the laser to a two-channel detection system.

Image rendering is accomplished by passing the signal read by the PMT to a computer. The output current from the PMT is fed into a discriminator circuit (F100-T, Advanced Research Inc.). The discriminator circuit is used to set a threshold to minimize background from the detector by adjusting a potentiometer. A low threshold means there is little noise in the system allowing most of the signal to be passed through the discriminator. The discriminator outputs a TTL pulse for each incident photon. A counter card on the computer reads the number of TTL pulses for each pixel displaying the TTL pulse count as signal intensity in the image.

If further image segmentation is required, or the spectral overlap of two fluorophores does not allow for proper separation as described earlier, a multichannel spectral imaging system can be implemented. In this case the two channel detectors are replaced with a Czerny-Turner spectrometer containing a 16-channel multianode PMT (R5900U-00-L16, Hammamatsu).

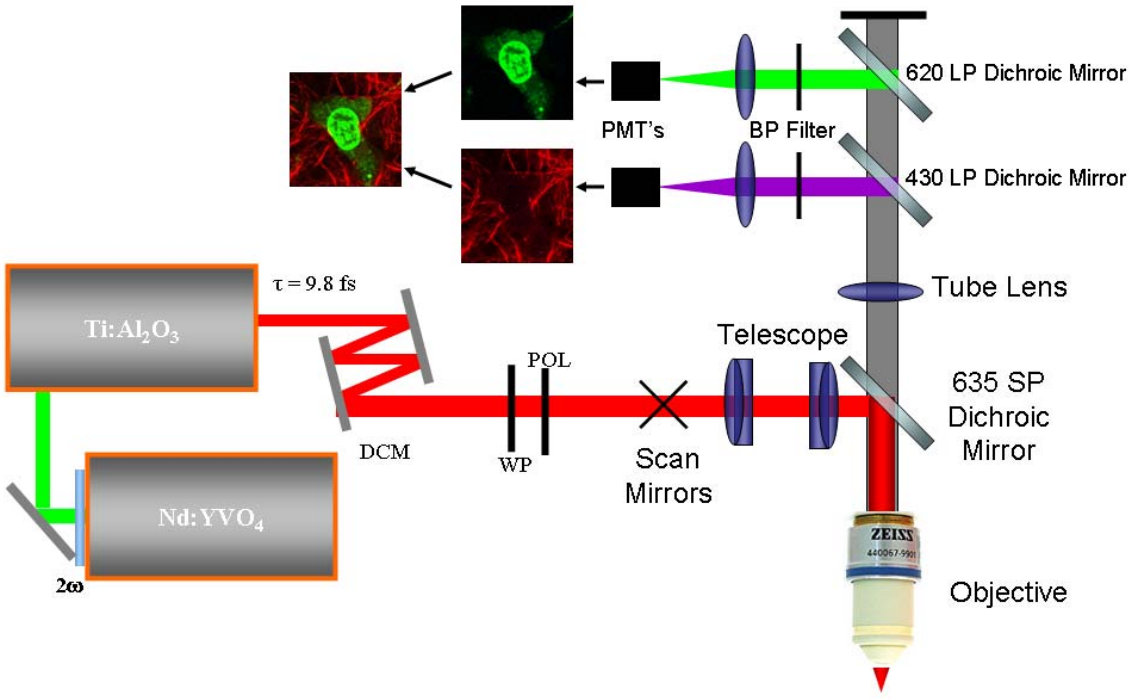

Fig. 2.10. Schematic of a NLOM. The laser is attenuated by the λ/2 waveplate (WP) and the linear polarizer (POL). The beam is directed to the scan mirrors through the telescope and reflected down to the objective by the primary dichroic mirror. Optical signals are collected by the objective and backscattered laser light is filtered by the primary dichroic mirror. Secondary dichroic mirros and bandpass filters (BP Filter) further segregate the collected signal into appropriate image channels. A lens focuses the signal onto the detector to minimize loss due to overfill.

A large core (910μm) multimode optical fiber is used to transfer the collected signal from the microscope to a remotely located spectrometer. The optical fiber is placed in a conjugate plane to the BFA. This creates a pivot point on the fiber aperture analogous to the pivot point of the scan mirrors on the BFA. Therefore, as the beam is scanned, the point on the fiber aperture is stationary. Configured in this manner, the core diameter of the fiber does not determine the field of view for the resulting image, rather, it determines the overall signal intensity. Field of view is determined by the acceptance angle, or NA (NA = 0.22), of the collection fiber. This layout is shown schematically in Fig. 2.11(A).

The optimal balance of sensitivity and resolution in a spectrometer comes from optically matching the entrance slit width to the exit slit width. The Czerny-Turner configuration chosen here places an image of the entrance slit onto the exit slit. In this system the entrance slit is defined by the fiber aperture and the exit slit by the physical width (0.8mm, 1.0mm pitch) of the detector elements. The 1.0mm pitch between elements means that overfilling the exit slit will result in a loss up to 20%. Divergent light from the entrance slit is collimated using the collimating lens of the spectrometer. The large fiber core diameter constitutes an extended source and necessitates a large diameter, long focal length (d=38.1mm, f = 90.0mm) collimating lens. To appropriately demagnify the entrance slit, a f = 75.0mm lens was used to focus the diffracted beam onto the detector. Spectrometer magnification is the ratio of focal lengths. The diffraction grating is placed in the infinity space between the two lenses and schematically shown in Fig. 2.11(B). Achromatic lenses corrected for the visible range were used in lieu of more common curved mirrors since off the shelf parts exactly matching system specifications were not readily available. Large diameter achromatic lenses have the advantage of well corrected spherical aberration which can lead to cross-talk between channels.

The diffraction grating is responsible for separating the collected beam into its individual spectral components. The diffraction angle is given by the grating equation

$$\sin(\alpha)+\sin(\beta)=md\lambda \qquad (2.35)$$

where α is the angle of incidence, β is the diffraction angle, m is the diffraction order, d is the groove density of the grating and λ is the wavelength of diffracted light. To obtain maximum diffraction efficiency from a blazed grating, the incident angle and diffracted angle should be equal. This condition is known as a Littrow configuration. In most cases it is not physically possible to have the entrance slit and detector spatially overlap. To overcome this drawback the plane of the grating is rotated 90° allowing the grating to be rotated perpendicular to the grooves. This rotation does not result in a loss of efficiency and allows the entrance slit and detector to be spatially separated. Next, we must determine the spectral extent that will fall on the detector from the known array width of 16mm. The linear dispersion of the spectrometer defines the spectral extent per unit width. Linear dispersion is given as

$$\frac{d\lambda}{dx} = \frac{\cos(\beta)}{mdL_B} = 17.58nm \qquad (2.36)$$

where L_B is the focal length of the focusing lens. A diffraction grating with 700 grooves/mm blazed at 530nm (53-067-455R, Richardson Grating) yields a spectral range of 280nm. The center wavelength of the spectrometer is set to 490nm giving a spectral range of 350-630nm. Spectral resolution is given by the pass band of the exit slit. The multianode PMT acts as a series of individual exit slits with a single element detector behind the slit. Exit slit pass band is given as

$$BP = \frac{w\cos(\alpha)}{mdL_A} = 14.22nm \qquad (2.37)$$

where w is the entrance slit width and L_A is the focal length of the collimating lens. The very low resolution and spacing between detector elements limits the impact of spectrometer aberrations on reduction in resolution.

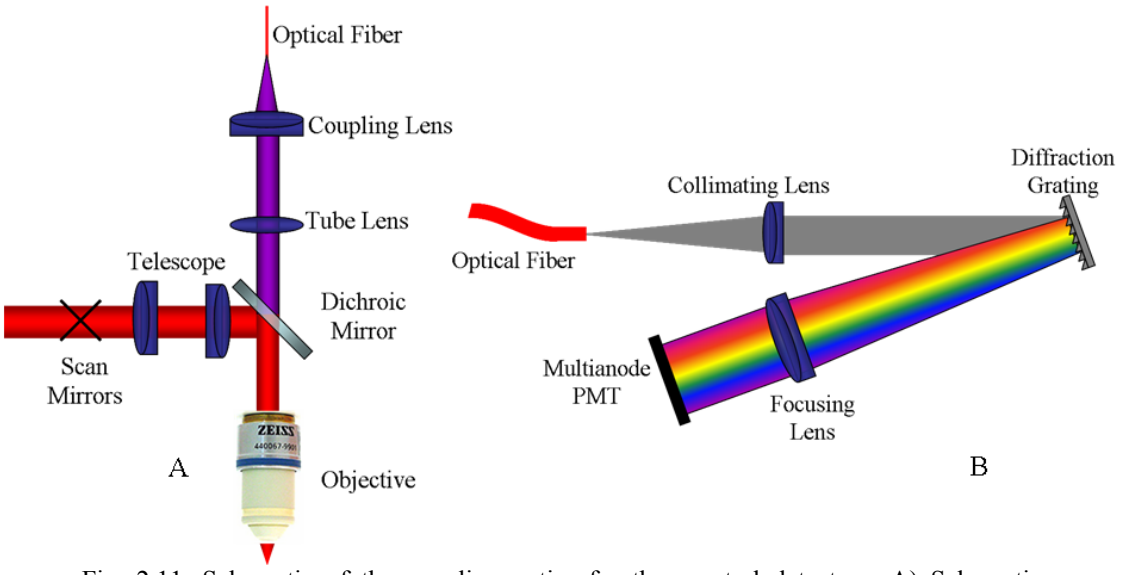

Fig. 2.11. Schematic of the coupling optics for the spectral detector. A) Schematic representation of the coupling optics necessary to focus the collected signal from the objective into the optical fiber. B) Optical schematic of the Czerny-Turner spectral detector. Light from the fiber is collimated by the collimating lens. Collimated light is then diffracted off the grating and focused onto the multianode PMT by the focusing lens.

Aberrations do not manifest themselves in the form of blur and distortion of an image as with light microscopy. Instead, aberrations result in a loss of excitation and detection efficiency. On the excitation side, spherical and chromatic aberration affect focal volume diameter and pulse distortions (Sec. 3.2). Flatness of field imparts a radial variation of the pulse duration at the focal plane owing to the radial varying dispersion profile of the optics (Sec. 3.2). Astigmatism does not affect the pulse shape or duration, however, it smears the axial point spread function reducing resolution. On the detection side, these aberrations will prevent photons from reaching the detectors reducing detection efficiency.

CHAPTER III
CHARACTERIZATION OF SUB-10-FS PULSES

This chapter discusses the temporal characterization of ultrashort pulses. Sec. 3.1 will encompasses dispersion, its effect on ultrashort pulses and methods for measuring ultrashort pulses. Sec. 3.2 will detail the temporal characterization of sub-10-fs pulses as they propagate through the microscope.

3.1 DISPERSION AND ULTRASHORT PULSE MEASUREMENT

3.1.1 Dispersion

Dispersion (a.k.a chromatic dispersion or material dispersion) is a material property manifested as the frequency dependence of the refractive index. The refractive index of a material is governed by $\chi^{(1)}$ susceptibility (Equation 1.1), which is proportional to material density and therefore results from the electromagnetic interaction of light waves with the bound states of the material. A frequency dependent refractive index has the additional consequence of imparting a frequency dependence on the velocity of light traveling through the material. This frequency dependent velocity (and therefore phase) is the mechanism that gives rise to temporal spreading of a laser pulse as it propagates through a material.

The refractive index of a material is given as

$$n = \sqrt{\varepsilon_r \mu_r} \tag{3.1}$$

where ε_r is the relative permittivity of the material and μ_r is the relative permeability of the material. For wavelengths far away from a material resonance (visible and near-IR for most glass), the refractive index can be approximated by the empirical Sellmeier equation

$$n(\lambda)^2 = \left[1 + \sum_{j=1}^{m} \frac{B_j \lambda^2}{\lambda^2 - C_j} \right] \tag{3.2}$$

where λ is the wavelength, B_j and C_j are experimentally determined Sellmeier coefficients typically expanded to $m = 3$. The calculated refractive index curve for fused

silica using Equation 3.2 is depicted in Fig. 3.1(A). The carrier envelope velocity of the optical pulse as it propagates through a material is termed the group velocity and is related to the refractive index by

$$v_g = c_0\left[n + \omega\frac{dn}{d\omega}\right]^{-1} \tag{3.3}$$

where c_o is the speed of light in a vacuum, n is the refractive index and ω is the frequency of light. From Equation 3.3 we can see that each frequency (and therefore wavelength) within the pulse will propagate at a different group velocity relative to the carrier envelope. This induces a phase shift, or group delay, for each of the spectral components as

$$\tau(\omega) = \frac{d\phi}{d\omega} = \frac{1}{c_o}\left[n + \omega\frac{dn}{d\omega}\right]L = \frac{2\pi L}{\lambda}\frac{dn}{d\lambda} \tag{3.4}$$

with L being the propagation length of the pulse in the material. The mechanism responsible for pulse broadening is the dispersion associated with the frequencies traveling at different phase velocities known as group delay dispersion (GDD). GDD is a function of the second derivative of the refractive index, therefore termed second-order dispersion, and is given by

$$GDD = \frac{d^2\phi}{d\omega^2} = \frac{1}{c_o}\left[2\frac{dn}{d\omega} + \omega\frac{d^2n}{d\omega^2}\right]L = \frac{\lambda^3 L}{2\pi c_o^2}\frac{d^2n}{d\lambda^2} \tag{3.5}$$

and is typically expressed in terms of fs^2. In the fiber optics community this term is normalized to a unit length following the derivative of the v_g termed group velocity dispersion (GVD). The calculated GVD curve for fused silica using Equation 3.5 is depicted in Fig. 3.1(B). In dealing with ultrashort pulses, it is often necessary to take into account higher order dispersion terms. For sub-10-fs pulses, third order dispersion (TOD) is usually sufficient and is given by

$$TOD = \frac{d^3\phi}{d\omega^3} = \frac{1}{c_o}\left[6\frac{d^2n}{d\omega^2} + \omega\frac{d^3n}{d\omega^3}\right]L = \frac{\lambda^4 L}{4\pi^2 c_o^3}\left(3\frac{d^2n}{d\lambda^2} + \lambda\frac{d^3n}{d\lambda^3}\right) \tag{3.6}$$

The calculated TOD curve for fused silica using Equation 3.6 is depicted in Fig. 3.1(C).

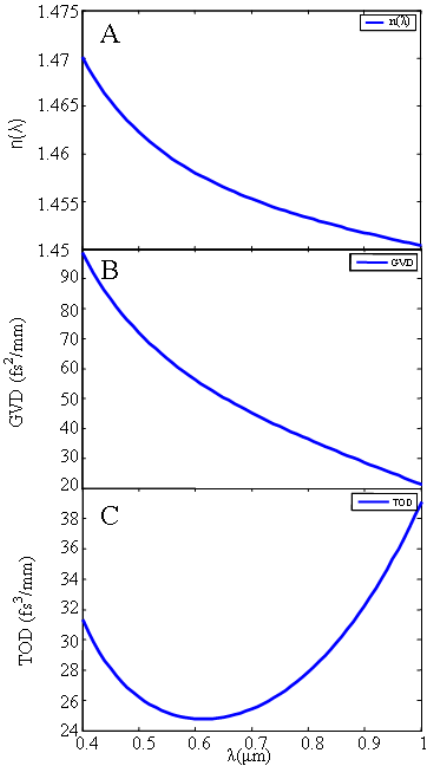

Fig. 3.1. Calculated dispersion curve of fused silica. A) Calculated refractive index curve for fused silica using the Sellmeier equation. B and C) Calculated GVD and TOD curves respectively for fused silica.

We can investigate the effects of dispersion on TPA and SFG by evaluating the electric field of the pulse and adding a phase term. For a *sech*^{2} pulse we have the electric field modulated by a phase term

$$E(\omega) = E_o \sec h^2(\omega) e^{i\phi(\omega)t} \tag{3.7}$$

where $E(\omega)$ is the Fourier transform of $E(t)$ and $\phi(\omega)$, the total frequency dependent phase shift, is defined by a Taylor expansion

$$\phi(\omega) = \phi(\omega_o) + \left(\frac{d\phi}{d\omega}\right)(\omega-\omega_o) + \frac{1}{2}\left(\frac{d^2\phi}{d\omega^2}\right)(\omega-\omega_o)^2 + \frac{1}{6}\left(\frac{d^3\phi}{d\omega^3}\right)(\omega-\omega_o)^3 + \ldots + \frac{1}{n!}\left(\frac{d^n\phi}{d\omega^n}\right)(\omega-\omega_o)^n \tag{3.8}$$

The quadratic dependence of □*(ω)* on second-order disersion imparts a linear ramp of frequency with respect to time imparting a linear chirp. The sinusoidal modulation on the frequency about the central frequency causes a reduction in the non-degenerate summation of intensity of the two-photon power spectrum *T(ω)* (Equation 2.16), therefore, proportionally reducing the probability of a two-photon transition described by Equation 2.17. For sufficiently large values of chirp elimination of all non-degenerate contributions can occur. Temporally speaking, different spectral components traveling at different group velocities smear the pulse in time, reducing the peak intensity of the pulse. A temporal smear decreases the probability that two photons whose energy summation satisfies the electronic transition of the fluorophore arrive at the same time. In terms of SFG, a reduction in the pulse intensity causes a reduction in the nonlinear source term of Equation 2.20. In the frequency domain, GDD, this amounts to a change in the wave vector increasing the wavevector mismatch.

The presence of TOD begins to change the shape of a pulse. This is because the central frequency arrives first followed by the frequencies on either side as a result of a quadratic dependence of group delay vs. frequency. Hence, TOD is sometimes referred to as quadratic chirp. Time delay in the arrival of spectral frequencies causes them to interfere resulting in beating seen in the temporal intensity profiles. Interestingly, this quadratic chirp effects *T(ω)* by narrowing the spectrum while maintaining amplitude. Amplitude is maintained because the non-degenerate frequency summations occur for the frequencies around the center remaining in phase. An identical narrowing of the sum-frequency spectrum is also seen, again due to wavevector mismatch.

3.1.2 Dispersion Compensation

We have seen in the previous section that uncontrolled phase distortions adversely affect the efficiency of the nonlinear processes involved in NLOM signal generation. Additionally, the increased bandwidth of temporally shorter pulses makes them more susceptible to the phase distortions introduced by the NLOM optical system, particularly through the use of high NA objectives.[77-81] For example, a 100fs pulse with 4000fs^2

GDD (a typical value for a nonlinear microscope) will be broadened to ~150fs whereas a 10fs pulse with the same GDD will be broadened to ~1.5ps. Efficient nonlinear signal generation with the least amount of power delivered to the specimen requires the compensation, or at least the minimization, of these phase distortions. Compression of 6-fs pulses was demonstrated by compensating GDD and TOD using a grating and prism sequence[82]. Previous works have examined the effects of ultrashort pulse propagation (ranging from 170-fs to 10-fs[9, 79, 80, 83, 84]) in NLOM optical systems and minimized phase distortions at the focal plane using prisms. Studies have also shown that the increased peak power of the pulse allows for enhanced depth penetration[5, 6, 8]. For very deep tissue imaging it may be advantageous to increase peak power through reduction in temporal duration instead of increasing pulse energy owing to the high susceptibility of ultrashort pulses to phase distortions mitigating out of focus signal generation generated when focusing 100nJ amplified pulses.

Dispersion compensation is accomplished by imparting a negative chirp equal to the positive chirp of the NLOM before it enters the microscope optics. In NLOM, the most common method of dispersion compensation is the use of a prism pair pre-chirper. In a prism prechirper light is incident on the first prism in the sequence at Brewster's angle. The dispersion of the prism causes the spectral components of the incident beam to exit the prism at different angles. A second prism is used to bring the dispersed beam back into parallel propagating beams where they are retroreflected back through the sequence as shown in Fig. 3.2. GDD for a prism sequence is given as

$$\frac{d^2\phi}{d\omega^2} = \frac{\lambda^3}{2\pi^2 c^2}\frac{d^2P}{d\lambda^2} \tag{3.9}$$

$$\frac{d^2P}{d\lambda^2} = 4\left[\frac{d^2n}{d\lambda^2} + \left(2n - n^{-3}\right)\left(\frac{dn}{d\lambda}\right)^2\right] l_p \sin(\beta) - 8\left(\frac{dn}{d\lambda}\right)^2 l_p \cos(\beta) \tag{3.10}$$

where $\frac{d^2P}{d\lambda^2}$ is a function of prism material, incident angle β, and prism spacing l_p.

TOD for a prism sequence is given as

$$\frac{d^3\phi}{d\omega^3} = \frac{-\lambda^4}{2\pi^2 c^3}\left(3\frac{d^2P}{d\lambda^2} + \lambda\frac{d^3P}{d\lambda^3}\right) \tag{3.11}$$

$$\frac{d^3P}{d\lambda^3} = 4\frac{d^3n}{d\lambda^3} l_p \sin(\beta) - 24\left(\frac{dn}{d\lambda}\frac{d^2n}{d\lambda^2}\right) l_p \cos(\beta) \tag{3.12}$$

where $\frac{d^2P}{d\lambda^2}$ is Equation 3.10 and $\frac{d^3P}{d\lambda^3}$ is again dependent on prism material, incident angle β, and prism spacing l_p. The drawbacks to a prism sequence are the requirement for long prism spacing large values of GDD (~45cm for 4000fs^2 using SF10 prisms) and net negative TOD. Large prism spacing can lead to an overfilling of the second prism face in ultrashort pulses owing to their large bandwidth. To counter the net negative TOD a grating sequence can be added. Grating sequences have the benefit of negative GDD but positive TOD. GDD for a grating pair is given as

$$\frac{d^2\phi}{d\omega^2} = \frac{\lambda^3 l_g}{\pi d^2 c^2}\left[1 - \left(\frac{\lambda}{d} - \sin(\gamma)\right)^2\right]^{-\frac{3}{2}} \tag{3.13}$$

and TOD is given by

$$\frac{d^3\phi}{d\omega^3} = \frac{-d^2\phi}{d\omega^2}\frac{6\pi\lambda}{c}\left[\frac{1 + \frac{\lambda}{d}\sin(\gamma) - \sin^2(\gamma)}{1 - \left(\frac{\lambda}{d}\sin(\gamma)\right)^2}\right] \tag{3.14}$$

where d is the groove spacing and γ is the angle of incidence on the grating.

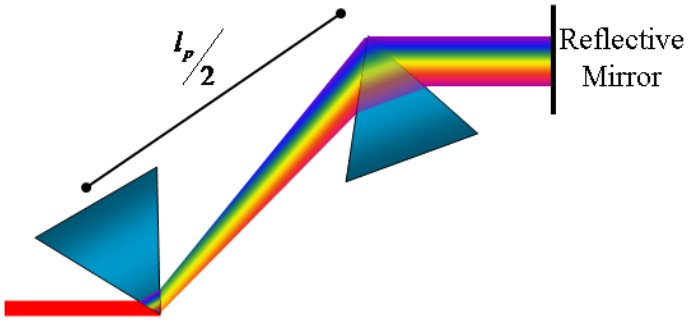

Fig. 3.2. Schematic detailing the principles of a prism prechirper. The incident beam is dispersed by the first prism in the sequence. A second prism makes the dispersed beams collinear where they are retroreflected back through the prism sequence. The retroreflector can be tilted slightly allowing the chirped pulse beam to be separated from the original beam.

Recent advancements in the development of double chirped mirror (DCM) technology have allowed the compression of ultrabroadband pulses in the single cycle regime[85]. Negative GDD and TOD is a function of a periodic series of selectively reflective layers. Phase shifts occur at the interface between the alternating high and low refractive index layers. Unlike conventional Bragg mirrors, DCM's have the added advantage of an increase in layer thickness the further into the stack light penetrates. This has the advantage of smoothing oscillations in the GDD curve that can occur in Bragg mirrors and allowing for dispersion compensation over a broader wavelength range. The selective reflectivity of the layer allows red frequency components to travel deeper into the chirped mirror stack accumulating a greater group delay relative to blue frequency components[86]. Further reduction in GDD oscillations is accomplished by using the first few layers of the mirror stack as an impedance matching series and an anti-reflection coating placed on the top layer. These layers prevent backreflections from the top and back mirror surfaces creating a Gire-Tournoise interferometer (GTI) inside the mirror stack. The multilayer structure of the DCM is schematically illustrated in Fig. 3.3.

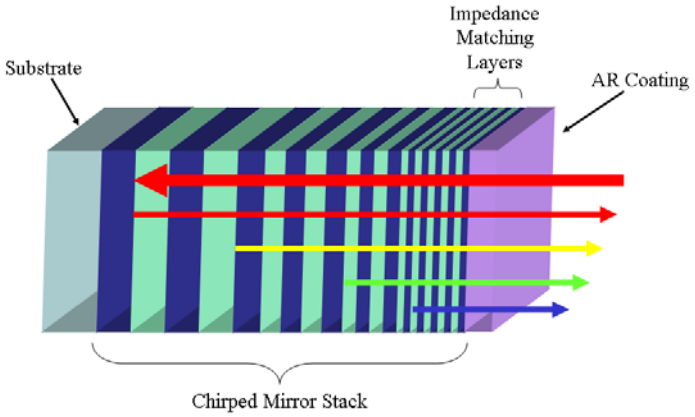

Fig. 3.3. Schematic of a chirped mirror stack. Alternating layers of a high index and low index material of increasing thickness provide phase delays across a broad spectral range. Dispersion compensation is a function of reflection through the mirror stack.

GDD and TOD are no longer a function of interelement spacing, but are functions of the multilayer mirror coating properties imparted per reflection. Negative dispersion can be added by increasing the number of reflections between a pair of CM's allowing for the construction of very compact dispersion compensation systems. The mirror layers can be designed to compensate for spectra spanning one octave[57]. Additionally, the TOD/GDD ratio can be customized to exactly compensate the dispersion of the optical system through which the laser will propagate[86]. This holds a distinct advantage over prism and grating based dispersion compensation methods. Furthermore, the nondispersive nature of the mirrors maintains beam quality.

3.1.3 Ultrashort Pulse Measurement

The high susceptibility of sub-10-fs pulses to dispersion mediated temporal broadening requires the ability to measure pulse width at the focal plane of the microscope. Measuring the pulse duration at the focal plane allows the pulse duration to be minimized as negative GDD is added to the system to compensate for the positive GDD of the optics in the microscope. This approach yields an exact GDD measurement of the microscopy system. Typically, this is done by a second-order interferometric

autocorrelation. The autocorrelation is termed second-order owing to the reliance on second-order nonlinear signals (i.e. SHG or TPA) for pulse width measurement.

Interferometric autocorrelations (IAC) are generated by placing a Michelson interferometer in the beam path. A beam splitter splits the beam into the two arms of the interferometer where they are retroreflected back and then recombined by the beam splitter into two overlapping collinear beams. The retroreflector in one of the arms is rapidly oscillated introducing an optical path difference, and therefore a time delay, between the two beams. Collinear beams are then focused into a nonlinear medium where they interfere[87]. The nonlinear medium is usually a KDP or BBO crystal to generate SHG. As we saw from Sec 2.2.3 the broad bandwidth of sub-10-fs pulses places a significant contstraint on second harmonic crystal thickness due to phase matching conditions. To minimize the influence of dispersion and phase mismatch from distorting the IAC, SHG crystals should be very thin (~25μm). SHG intensity is then integrated by a photodetector as a function of time delay. The beam path is illustrated in Fig. 3.4. The general expression for the IAC is given as

$$I_{IAC} = \int_{-\infty}^{\infty} \left| E(t) + E(t-\tau)^2 \right|^2 dt = \int_{-\infty}^{\infty} \left| E(t)^2 + 2E(t)E(t-\tau) + E(t-\tau)^2 \right|^2 dt \qquad (3.15)$$

For long delays the intensity read by the photodetector is the sum of the SHG produced by each pulse pair and defines the background as

$$I_B = \int_{-\infty}^{\infty} \left| E(t)_1^2 \right|^2 + \left| E(t-\tau)_2^2 \right|^2 = 2\int_{-\infty}^{\infty} \left| E(t)^2 \right|^2 \qquad (3.16)$$

In the case of zero delay between the two pulses we get the coherent superposition of the of the two fields

$$I(0) = 16\int_{-\infty}^{\infty} \left| E(t)^2 \right|^2 \qquad (3.17)$$

leading to the characteristic 8:1 contrast ratio of the second-order IAC. When the two pulses are delayed such that the field maximum of one pulse and the first minimum of the electric field from the second pulse are aligned near complete destructive

interference occurs between the two fields creating a zero intensity read by the detector illustrated in the IAC curve of the sub-10-fs laser in Fig. 3.4.

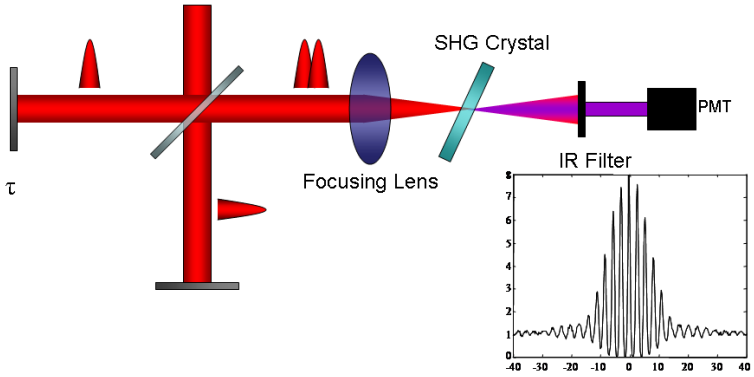

Fig. 3.4. Schematic illustration of a second-order interferometric autocorrelator. Inset: IAC of a sub-10-fs pulse laser.

Second order IAC can also be obtained through TPA. In this configuration, the collinear beams are focused into a fluorescent dye solution[79] or onto a two-photon absorbing photodiode[88]. Using a fluorescent dye or two-photon absorbing photodiode can be advantageous in measuring ultrashort pulses over second harmonic crystals as they are not subject to phase matching conditions. Additionally, two-photon photodiodes have been shown to have a wider spectral response than a second harmonic crystal making them well suited to sub-10-fs pulse width measurements.

A drawback to the IAC arises in deviations in pulse shape from a complex spectral phase profile can cause an inaccurate measurement of pulse width. This makes the IAC better suited to measuring transform-limited or near transform-limited pulses, that we obtain at the focal plane of a microscope with proper dispersion compensation. To obtain complex spectral phase information it is necessary to measure a pulse in time and frequency simultaneously (the time-frequency domain) using Frequency-Resolved Optical Gating (FROG)[89, 90] and Spectral Phase Interferometry for Direct Electric-Field Reconstruction (SPIDER)[91, 92].

3.2 *EX VIVO* CHARACTERIZATION OF SUB-10-FS PULSES

Characterization of sub-10-fs pulses through the NLOM optical system is an integral step in generating efficient nonlinear optical signals from within biological specimen. Nonlinear signal generation falls off rapidly as spatial, and temporal distortions affect pulse parameters. The phase fronts leading each spectral component are no longer superimposed on one another reducing the peak power of the pulse and altering its shape. Therefore, it is necessary to compensate for this by imparting a negative linear chirp that is equal or nearly equal to the positive linear chirp imparted by the glass of the optical system.

In our system, schematically shown in Fig. 3.5, phase distortions of sub-10-fs pulses propagating along the optical axis were corrected using a pair of dispersion compensating mirrors (DCM). Pulses were characterized by inserting a low dispersion Michelson interferometer into the optical path allowing collinear beams to be directed to the microscope. Collinearly propagating beams allows the pulse to be characterized across the entire aperture of the optical system under test. The laser is coupled into the epi-fluorescence port of the microscope via the galvanometer driven mirrors. A 1.5:1 beam expanding telescope comprised of two near-IR designed achromatic lenses appropriately images the spot from between the galvanometer mirrors to the back focal aperture (BFA) of the microscope objective. The beam is directed to the microscope objective by the primary dichroic mirror. The objective focuses the collinear beams into a piece of mouse tail tendon (MTT) immersed in phosphate buffered saline (PBS). MTT is primarily composed of collagen fibers and is used as the $\chi^{(2)}$ crystal to generate the IAC. Nonlinear optical signals are collected by the focusing objective and directed to the two channel detector unit mounted on the trinocular head. Back scattered laser light was filtered during autocorrelation measurements using 1 mm of BG-39 Schott glass filter.

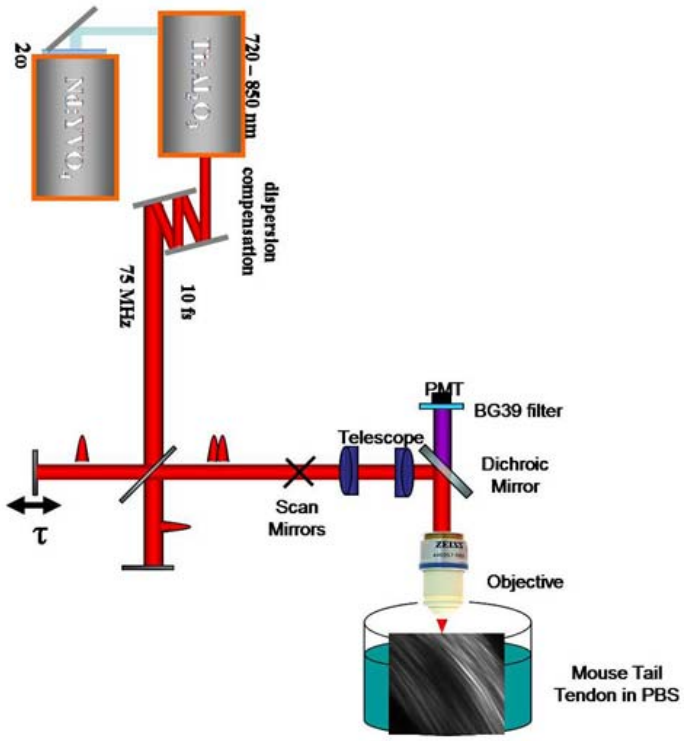

Fig. 3.5. Schematic diagram for *ex vivo* pulse characterization. Illustrated are the laser, dispersion compensation optics, autocorrelator, scan telescope and microscope optics.

This arrangement allows the measurement of the pulse after propagating through all components of the optical system including the multilayer dielectric coating of the primary dichroic mirror and the immersion medium. The dielectric layers of the dichroic mirror will impart a frequency chirp similar in nature to the DCM. The proper objective immersion medium is required to account for its added dispersion to the optical system and for appropriate control of aberrations in the objective lens, stemming the use of MTT immersed in PBS. MTT was chosen as the medium to generate the second order signal in order to characterize pulse behavior within a common biological constituent. Intensity of SFG signal generated within MTT is proportional to the spectral upconversion within the collagen. The ability to generate short autocorrelations within the MTT indicates near entire upconversion of the pulse spectrum for maximum

signal generation. Autocorrelations generated in MTT have identical pulse width to those obtained with a GaAsP photodiode (Fig. 4.5 (B)).

The double-pass configuration of DCM allows a total of 32 bounces. This geometry gives simple dispersion tuning up to -6400 fs^2 and -3840 fs^3 in increments of -400 fs^2 and -240 fs^3 in GDD and TOD, respectively, at 800 nm with 82% (94% if retro-reflector losses are neglected) efficiency after 16 bounces. Fixed negative chirp imparted by DCM per reflection requires addition of glass to the beam path for fine dispersion compensation adjustments. We use combinations of antireflection coated BK7 windows at 2, 3, or 4 mm thickness and fused silica wedge pair, each mounted on a linear translation stage providing an additional 400 μm to 3 mm of glass. This corresponds to precise control of up to 518.2 fs^2 GDD and 375 fs^3 TOD.

Autocorrelation traces in Fig. 3.6(A-F) show distinctive side lobes on either side of the central peak. FWHM of the central peak is reported as Minimum Pulse Width assuming a $sech^2$ pulse shape (see Table 3.1). Side lobes are the result of cross correlation between a broadened, marginal ray and an optimally compensated pulse traveling along the optical axis at the paraxial focus[81]. Delay between the central and side lobe peak is associated with chromatic and spherical aberration within the optical system.[93] This is reported as Total Delay in Table 3.1 and indicates the delay for pulses passing radially through the system. The values of Total Delay are consistent with previously reported studies[81].

Unfortunately, the optics of the system have aberrations and therefore impart a nonuniform phase delay across the aperture of the optic. It has been reported[77] and experimentally shown[94] that significant pulse broadening can occur because of non-constant GDD across the face of a lens leading to propagation time difference (PTD). The curvature of a positive lens dictates that the central portion of a lens be thicker than the periphery. This means that we now have a spatial distribution of dispersion and a radial dependence on the position in time and space of the pulse traveling along the optical axis as compared to a marginal pulse. For a given frequency, a marginal pulse will arrive at the paraxial focus before a pulse traveling along the optical axis arising in

propagation time difference (PTD) causing an artificially broad pulse to arrive at the focus. These distortions can not be compensated by traditional means and would require the fabrication of a pre-chirper with a radially varying chirp. Achromatic lenses correct for this type of distortion as the optical path length across the face of the lens is constant for a given frequency. There is still, however, a frequency component to PTD in achromatic lenses as they can not be made perfect for all spectral components. The objective lenses for this microscope are chromatically corrected for the visible region which will lead to some PTD broadening when illuminated with NIR light. The curvature of a lens system will also induce spherical aberration when marginal pulses are refracted to a higher degree, owing to a greater curvature near the periphery, than pulses near the optical axis. This causes marginal pulses to come to a focus before the paraxial focus. Spherical aberration in conjunction with spherochromaticity lead to the formation of a pre-pulse.

An interferometric autocorrelation in Fig. 3.6(G) obtained using 20X Plan-Apochromat, 0.75NA (Zeiss) air objective collimated by a near-IR achromat outside the microscope with a beam diameter relative to BFA was $D_r = 0.32$ does not show side lobes. FWHM of 11.5 fs compared to 11.7 fs for the identical objective using MTT at $D_r = 0.7$ (Fig. 3.6(A)) justifies the Minimum Pulse Width. The effects of spherical and chromatic aberration can be minimized for $D_r < 0.4$ allowing one to obtain the original pulse width.[81] With $D_r > 0.4$, aberration increases quadratically with radial distance. The actual pulse width of a 10-fs laser has been measured at the paraxial focus of a singlet lens with chromatic and spherical aberrations[78]. Furthermore, such aberrations are responsible for distortions in the spatial field at the focus[95].

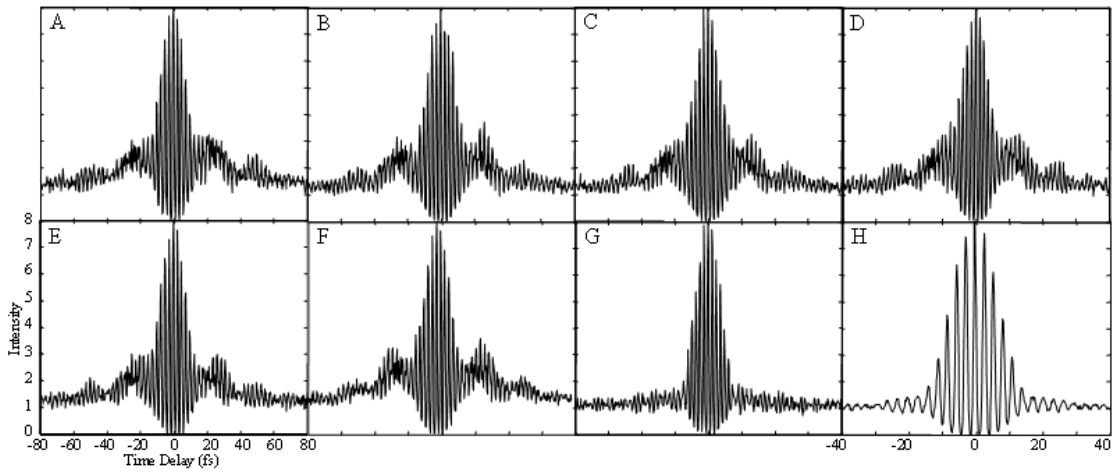

Fig. 3.6. Interferometric autocorrelation at NLOM focal plane. A) 20X Plan-Apochromat 0.75 NA, B) 20X Achroplan 0.5 NA, C) 40X Achroplan 0.8 NA, D) 63X Achroplan 0.95 NA, E) 100X Achroplan 1.0 NA, F) 63X C-Apochromat 1.2 NA, G) 20X Plan-Apochromat .75 NA with small beam diameter, and H) Sub-10-fs pulse directly from oscillator for reference.

The Achroplan series of objectives all share similar spherical and chromatic aberration. The 20X Plan-Apochromat shows the least amount of total delay with minimum objective contribution to aberration while realizing the full aberration induced by the telescope. The 63X C-Apochromat, 1.2 NA shows the shortest total delay with an overfilled aperture, indicating its higher level of aberration correction. Aside from the 100X Achroplan, 1.0 NA, the two most well corrected objectives yield the shortest minimum pulse width. The 100X Achroplan yields shortest pulse widths because it has the least amount of dispersion to compensate, and thus, the smallest residual TOD. Pulse width calculations, optic dispersion parameters and D_r for each objective are presented in Table 3.1.

Table 3.1. Measured pulse parameters at the NLOM focal plane. Calculated dispersion parameters, minimum pulse width(±.4 fs), BFA (D_r) and total delay (±2.7 fs) of the pulse.

Component	GVD (fs^2)	TOD (fs^3)	Minimum Pulse Width (fs)	D_r	Total Delay (fs)
20X Achroplan 0.5NA	-3818.7	-2378.4	12.5	1.0	26.5
40X Achroplan 0.8NA	-4000.0	-2400.0	12.7	0.7	25.4
63X Achroplan 0.95NA	-3728.0	-2367.6	12.3	1.0	26.5
100X Achroplan 1.0NA	-3464.0	-2143.8	11.3	1.4	26.5
20X Plan-Apochromat 0.75NA	-3728.0	-2367.6	11.7	0.7	21.1
63X C-Apochromat 1.2NA	-4528.0	-2847.6	11.9	1.2	25.1

3.3 CONCLUDING REMARKS

We have demonstrated the ability to compensate phase distortions induced by ultrashort pulse propagation through a complete NLOM optical system. To our knowledge, this is the first time aberration and dispersion has been characterized in a NLOM optical system using sub-10-fs pulses. The ability to obtain minimally broadened pulses within a MTT preparation indicates that nearly the entire pulse spectrum is being upconverted and phase matching condition is significantly relaxed. The measurement of minimally broadened pulses at the focal plane of the NLOM is essential for live tissue imaging by minimizing thermal and photo damage mechanism. Additionally, the entire pulse spectrum is available at the focus of the NLOM allowing for multiple fluorophore excitation. New capabilities may be realized with NLOM utilizing dispersion compensated ultrashort pulses including efficient, simultaneous excitation of multiple fluorophores for optical molecular profiling and laser microsurgery[96-98] without pulse amplification.

CHAPTER IV
MULTISPECTRAL NONLINEAR OPTICAL MICROSCOPY

This chapter discusses the simultaneous excitation of multiple fluorescent probes in NLOM. Sec. 4.1 details the advantages of multispectral imaging in further understanding biological processes. Sec. 4.2 discusses multiple fluorophore excitation using sub-10-fs pulses. Sec. 4.3 demonstrates the multispectral imaging capabilities of NLOM using an *in vitro* angiogenesis model.

4.1 MULTISPECTRAL NONLINEAR OPTICAL MICROSCOPIC IMAGING

Optical molecular imaging is an emerging field comprising several techniques to provide complimentary information at the molecular, cellular, tissue, and whole-organism levels[10]. These techniques are well matched with emerging genomic and proteomic technologies[1, 11] enabling the development of fluorescent (protein) optical probes[12] and nanotechnologies allowing multifunctional imaging in real time with minimal or no invasion[13, 14]. The minimally invasive nature of nonlinear microscopic imaging and its ability to provide concomitant morphological and chemo-physiological information within tissues makes it well suited to follow the developmental progression and response to pathologic or mechanically induced stressors. Additionally, the wide range of detectable contrast mechanisms available to NLOM make it well suited to optical molecular imaging from the nano to macro scale.

The advantages of nonlinear signal generation for imaging vary depending on the tissue and mechanism of signal generation. Second harmonic generation (SHG) requires highly ordered tissue structures, making it a constituent specific intrinsic contrast mechanism localized to collagen[15-17], cardiac myocites[18] and muscle sarcomeres[19]. Two-photon excited autofluorescence of NAD(P)H[20-26], flavins[27], and mature elastin[28] provides morphological, spectroscopic and metabolic information surrounding cellular processes. Morphological and functional imaging can be further expanded with the use of exogenous markers specific to tissue

constituents[99]. Fluorescent proteins are increasingly being used to observe developmental events as they can be widely expressed in the cytoplasm or inserted into genes for specific cytogenetic profiling. Efficient interpretation of these contrast mechanisms requires multispectral imaging capabilities.

The primary complication to *in vito* nonlinear multispectral imaging is the reliance on narrowband femtosecond laser pulses. Optimal fluorescence excitation efficiency necessitates the tuning of the laser to an absorption maximum for the individual contrast agents and rescanning of the tissue. To overcome this drawback, we use broadband, sub-10-fs pulses having a spectral bandwidth of ~125 nm. Two-photon excitation efficiency is determined by the overlap of the laser two-photon excitation power spectrum and the two-photon action cross section of the fluorescent probe of interest[1]. Sub-10-fs pulses therefore, require careful control of the pulse duration at the sample. The minimization of pulse duration at the sample[9], allows the contribution of all spectral components to fluorophore excitation. Furthermore, simultaneous excitation of multiple contrast agents greatly reduces the photo and thermal damage associated with rescanning the sample. An *in vitro* angiogenesis model[100] using human umbilical vein endothelial cells (HUVEC's) expressing multiple (Cyan, Green, Yellow, DsRed) fluorescent proteins was used to demonstrate the viability of broadband excitation in multispectral NLOM.

4.2 CHARACTERIZATION OF SUB-10-FS PULSE INTERACTIONS WITH COMMON DYE SOLUTIONS

Pulse characterization in dye solutions are also necessary to fully understand the TPA process. Dye solutions were not used to characterize pulse width and optical properties of the NLOM system, but rather the ability to excite multiple fluorophores simultaneously having well separated two-photon absorption profiles with sub-10-fs pulses. Efficient simultaneous excitation of multiple fluorophores reduces the photodamage inherent to multiple fluorophore experiments using narrowband pulses. Narrowband pulses for excitation require the laser to be tuned and the sample rescanned

for each of the fluorophores used. To avoid detrimental effects of photo and thermal damage inherent to rescanning, the laser is often tuned to a compromising wavelength and the power increased giving rise to simultaneous inefficient excitation. Given the broad bandwidth of sub-10-fs pulses, all fluorophores in the visible range can be simultaneously and efficiently excited using a single pulse.

Two-photon excitation cross-sections and emission spectra of common organic dyes and green fluorescent proteins using ~100 fs pulses has been measured[101-103]. These studies indicate that there are large two-photon excitation cross sections throughout the Ti:Al_2O_3 tuning range among many of the common dyes used in fluorescence microscopy. This makes many of the commercially available dyes suitable for NLOM. Two-photon absorption spectra were measured using a 170 fs narrowband Ti:Al_2O_3 laser as a function of fluorescence emission intensity vs. central wavelength tuning, Fig. 2.6, for three common biological fluorophores Indo-1, FITC, and TRITC. From our discussion in Sec. 2.2.2, it should be possible to excite all three of these dyes simultaneously using a sub-10-fs pulse.

In order to test the ability to excite multiple fluorophores simultaneously, transform limited sub-10-fs pulses were focused using a f=50mm curved mirror just beyond the wall of a Schott B270 (German white soda glass) cuvette with all sides polished. Laser beam attenuation was accomplished by rotating the first of a pair of crossed polarizers such that the output polarization remained constant. A total of -300 fs^2 GDD was imparted on the pulse using DCM's to compensate for the oscillator, polarizers and cuvette wall evidenced by the 10.4 fs autocorrelation obtained with similar system parameters in Fig. 4.1. A curved mirror was chosen for focusing over an achromatic lens as it does not introduce additional dispersion or chromatic aberration which can lead to pulse distortions.

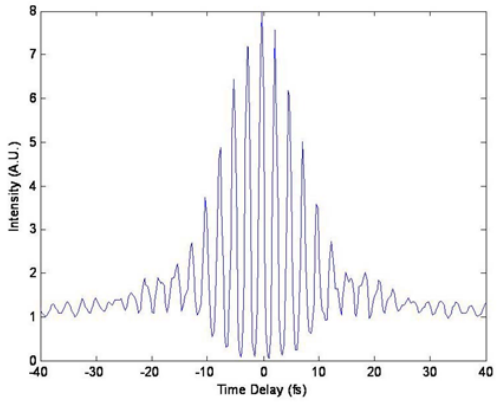

Fig. 4.1. 10.4 fs autocorrelation of the pulse focused just within the cuvette.

Dye solutions comprised of Indo-1, FITC, and TRITC were chosen as their emission spectra cover most of the visible range. To ensure TPA for the individual dyes, an emission spectrum, Fig 4.2(B, bottom), was collected as the input power was varied from 10-100 mW in 10 mW increments. The peak fluorescence at each power level vs. incident laser power was plotted to verify an I^2 power dependence for each dye tested. The one-photon absorption (OPA), one-photon emission peak (OPE) and two-photon emission peaks (TPE), dye concentration, solvent, I^2 slope and R^2 value for each dye are detailed in Table 4.1.

Table 4.1. Emission, concentration, solvent and intensity slope of the dyes under test.

Dye	OPA	OPE	TPE	concentration	Solvent	I^2 slope	R^2
Indo-1	345 nm	475 nm	498 nm	100μM	Water	2.00 ±.02	.998
FITC	496nm	518 nm	531 nm	100μM	Water	2.00 ±.02	.999
TRITC	552 nm	577 nm	582 nm	100μM	MeOH	1.93 ±.01	.999

Each dye exhibited a notable red shift in the emission spectra over their one photon counterparts. Indo-1 showed a distinctly larger red shift over FITC and TRITC. Simultaneous excitation of Indo-1, FITC and TRITC in a mixed solution is shown in Fig. 4.2(B, top). The narrowed and reduced spectrum of Indo-1 in this plot is believed to result from one-photon absorption of Indo-1 fluorescence by FITC. The one photon

absorption spectra of FITC and TRITC are illustrated in Fig. 4.2(A). The valley between Indo-1 and FITC emission corresponds with the one-photon absorption peak of FITC. We can also see that the valley between FITC and TRITC corresponds with the one-photon absorption peak of TRITC.

The FITC emission peak of the Indo-1 and FITC mixture (Fig 4.2 (B, middle cyan)) is blue shifted with regard to the two-photon emission peak of the individual solution of FITC outlined in green (Fig. 4.2(B, bottom green)). The individual dye solution of TRITC (Fig. 4.2(B, bottom red)) and the simultaneous Indo-1 and TRITC (Fig. 4.2(B, middle purple)) curve have similar Indo-1 profiles, though a slight blue shift of the TRITC spectrum. This shift is most likely due to TRITC being added to water, a change in the grating position of the spectrometer between the two curves and a slight contribution of Indo-1 fluorescence. Blue shift of TRITC becomes more pronounced in the simultaneous excitation of all three dyes and can be attributed to the FITC emission tail.

4.3 MULTISPECTRAL IMAGING USING AN *IN VITRO* ANGIOGENESIS MODEL

HUVEC's (Cambrex) were grown on gelatin-coated tissue culture flasks (1mg/ml) in culture media that consisted of M199 containing 15% fetal bovine serum, 400ug/ml bovine hypothalamic extract [104], 100ug/ml heparin (Sigma), 0.1% gentamycin and 1% penicillin/streptomycin (Invitrogen). Cells were passaged once a week and used between passage 2 and 6. Stable cell lines expressing the fluorescent proteins previously detailed were generated using a recombinant lentivirus system (Invitrogen). Backbone plasmid (4ug) and Virapower plasmid (12ug) was transfected into 293 FT packaging cell line (Invitrogen) using 36ul Lipofectamine 2000. Supernatants were collected at 72 hours, centrifuged at 500Xg for 10 minutes, filtered and used fresh to transfect passage 2 cells. Following blasticidin selection (5ug/ml) for 2 weeks, cells were frozen down at passage 3 or used in experiments.

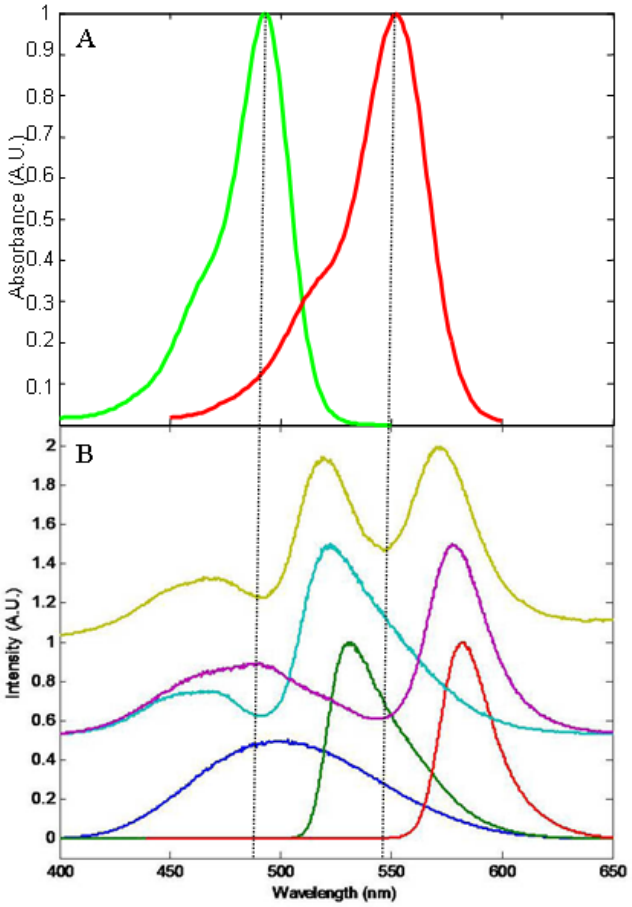

Fig. 4.2. Absorption and emission spectra of three biological fluorophores. (A) One-photon absorption spectra of FITC and TRITC. (B) Top: Simultaneous excitation of Indo-1, FITC and TRITC, Middle: Simultaneous excitation of Indo-1 and FITC (cyan) Indo-1 and TRITC (purple), Bottom: Individual emission spectra of Indo-1 (blue), FITC (green), and TRITC (red). Dashed vertical lines indicate the one-photon absorption peak of FITC and TRITC.

Fibrous collagen gels (3.6mg/ml, BD Biosciences) were assembled as previously described [105] before incorporating 1μM S1P. After thorough mixing, 1ml of collagen mixture was added per well of a Falcon 12-well plate (Becton Dickinson). Gels were allowed to polymerize and equilibrate for 20 minutes at 37°C in CO_2 incubator prior to seeding $3.6x10^5$ cells per well in serum-free Medium 199 (Invitrogen) containing reduced serum supplement II (RSII), recombinant VEGF (40ng/ml, Upstate Biotechnology), recombinant FGF (40ng/ml), ascorbic acid (50μg/ml) and TPA

(50ng/ml, Sigma Aldrich). After allowing ECs to attach to the collagen matrix for 20 minutes, the seeded gels were covered with 3ml of identical serum-free media. For imaging the media was removed and replaced with PBS. After images were acquired PBS was replaced with media and the cultures were placed back in the incubator.

A key advantage to NLOM is the reduced photobleaching and photodamage associated with the generation of observable optical signals being confined to the focal plane. Broadband NLOM represents a greater reduction in thermal and photodamage of multiply labeled tissue cultures by exciting all fluorescent molecules simultaneously. As we have previously stated, this allows for the signal (and therefore, spectra) of all constituents to be collected simultaneously without the need to tune the laser and rescan the tissue. During each imaging session, two or three lumen were imaged sequentially. For each lumen an image stack was obtained ranging from 60 μm to 180 μm in depth. A 2μm interval between slices was used to minimize the time tissues were left out of the incubator. Each slice was reconstructed from three scans (16 s per scan) using 40 mW of power to the galvanometer mirrors. The progression of the cells over 24 hours indicates that the long scan duration did not damage the tissue over the imaging period.

Reference spectra for the individual fluorescent proteins were obtained by imaging a confluent monolayer of HUVEC's seeded directly onto the bottom of a Falcon 12-well plate. The obtained reference spectra are normalized to peak fluorescence intensity and shown in Fig. 4.3. Emission spectra are clearly separated and well defined. The image corresponding to the 60 hour time point was chosen as it contains HUVEC's expressing three (cyan, green, yellow) of the four fluorescent proteins. We were unable to obtain a single lumen that contained cells expressing all four fluorescent proteins. The spectra for a region of interest corresponding to collagen, individual cells, and the lumen are shown in Fig. 4.4. The regions over which the spectra were integrated are outlined with a dashed box. Fluorescence intensity for the obtained spectra are normalized over the number of pixels within the dashed box prior to image processing. Therefore, the fluorescence intensities can be compared on a relative basis.

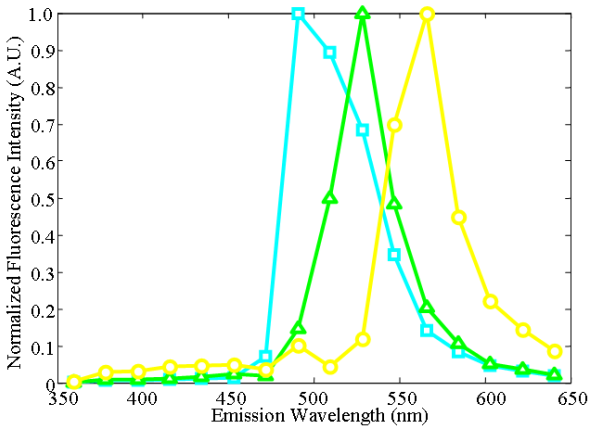

Fig. 4.3. Emission spectra of three fluorescent probes. Emission wavelength of Cyan fluorescent protein (cyan, square) Green fluorescent protein (green, triangle) and yellow fluorescent protein (yellow, circle) collected using the spectral detector.

Second harmonic wavelengths corresponding to the extracellular matrix are represented in region one and corresponds to the expected peak near 400 nm. Spectra in regions two through four represent the individual fluorescent proteins expressed by the HUVEC's. The spectral peaks of the *in vitro* experimental spectra correspond well with their reference counterparts. A final spectrum within the lumen was extracted indicating very low signal levels that appropriately correspond to background signal.

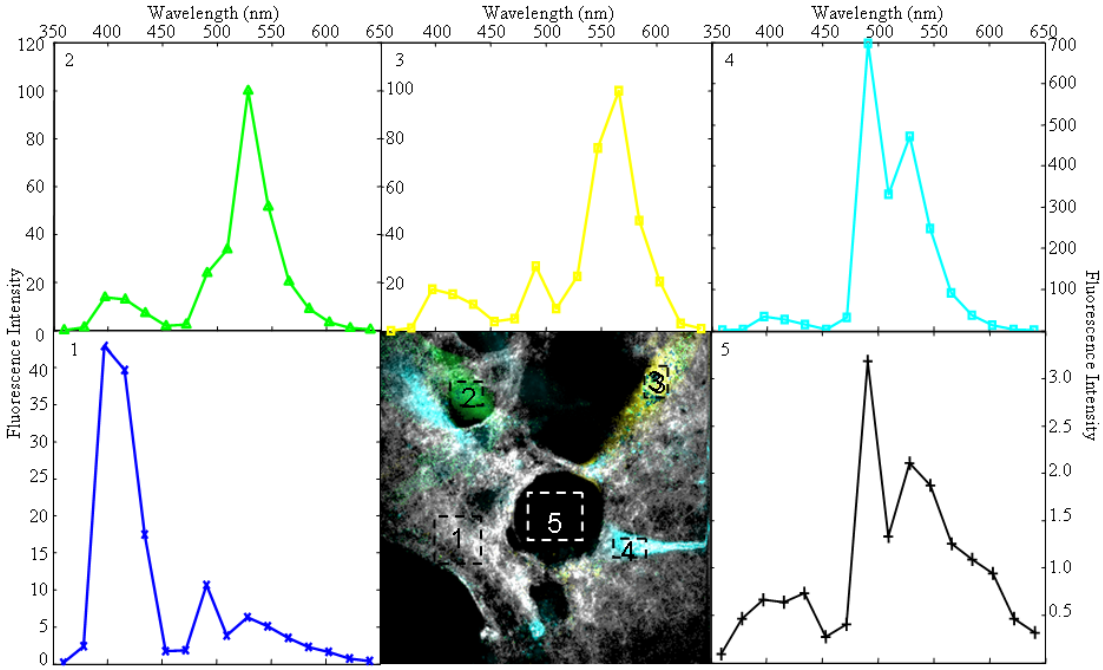

Fig. 4.4. Emission spectra obtained from regions of interest within an image. The lumen is expressing cyan, green and yellow fluorescent protein. Spectra are representative of 1. Second harmonic generation. 2. Green fluorescent protein. 3. Yellow fluorescent protein. 4. Cyan fluorescent protein. 5. No signal in the lumen.

4.4 CONCLUDING REMARKS

The data clearly indicate broadband sub-10-fs pulses are capable of exciting multiple fluorescent proteins simultaneously. Long term, time lapse imaging was demonstrated with negligible damage to the tissue culture. Changes in cell morphology and location can be seen through the time progression of images. Individual spectra for the expressed fluorescent proteins can be obtained from a region of interest. These spectra compare well to the reference spectra taken outside the tissue model. Our data indicate that multiple fluorescent proteins can be excited simultaneously and discriminated spectrally in the final image. This study motivates the future use of fluorophores or fluorescent proteins to examine integrin and adhesion molecule expression of HUVEC's as they correspond to angiogenesis for better understanding of the underlying processes of cell-matrix interaction in lumen growth. Furthermore, this work can be extended to myriad

of biological systems looking to investigate the progression and development of a system over time.

CHAPTER V
OPTICAL FIBER DELIVERY OF SUB-10-FS PULSES

This chapter details the propagation of ultrashort pulses through optical fibers. Sec. 5.1 starts with a discussion on the confinement of light within an optical waveguide and a discussion on different fiber types. Sec. 5.2 encompasses the selection of an appropriate optical fiber for ultrashort pulse delivery and characterizes the propagation of ultrashort pulses through optical fiber for use in NLOM.

5.1 CONFINEMENT OF LIGHT IN OPTICAL WAVEGUIDES

Optical fibers represent a class of structures capable of guiding light through a flexible medium. This is in contrast to how light propagates in air where it must travel in a straight line until its direction is changed by a scattering event or the beam of light encounters an intense gravitational field. It was demonstrated in the mid 1800's that light could be guided through a curved stream of water or curved glass rod by total internal reflection. The first guiding of light in an uncladded fiber wasn't demonstrated until the 1920's with the first cladded optical fibers being developed in the 1950's as coherent image guides. It was not until the advent of the laser, however, that fiber optic technology began to develop. The first single mode fiber was demonstrated in 1966. As fiber losses began to be reduced with better manufacturing and design, nonlinear optical processes were observed in the early 1970's.

Step-index optical fibers are characterized by a high refractive index core surrounded by a lower refractive index cladding that insures the confinement of light by total internal reflection (TIR). The core and cladding are arranged concentrically and share cylindrical symmetry illustrated in Fig. 5.1. The core diameter and ratio of refractive indices define the confinement parameters of the optical fiber. TIR occurs at the interface of two different dielectric media when the angle of incidence is greater than the critical angle defined as

$$\theta_c = \sin^{-1}\left(\frac{n_{clad}}{n_{core}}\right) \tag{5.1}$$

where n_{clad} is the lower refractive index material and n_{core} is the higher refractive index material. The angle of acceptance (NA) for an optical fiber is dictated by the critical angle and is given by

$$NA = \sqrt{n_{core}^2 - n_{clad}^2} \tag{5.2}$$

meaning that rays incident at a higher angle will not be totally internally reflected and are lost into the cladding. The number of modes supported by a fiber can found by using the *V*-number

$$V = \frac{2\pi}{\lambda} aNA \tag{5.3}$$

where *a* is the core radius, λ is the wavelength, and NA is defined by Equation 5.2. A fiber is said to be single mode (TEM_{00} mode) for wavelengths whose *V*-number <2.405 which corresponds to the first zero for a zero order Bessel function of first kind and contains a Gaussian mode profile. For a given core radius and NA of an optical fiber being used, wavelengths which correspond to a *V*-number >2.405 propagate at higher spatial mode orders. Single mode propagation is essential for stationary phase fronts necessary to eliminate modal dispersion. Modal dispersion is the property of an optical fiber where different modes propagate at different group velocities which can lead to uncontrollable temporal broadening in ultrashort pulses. Fig. 5.2 shows the *V*-number with respect to wavelength calculated for the fiber properties (*a*=2.25μm NA=0.13) used in this work. The cutoff wavelengths for higher order modes are indicated with solid lines. The intensity of the transverse modes are shown in the appropriate regions.

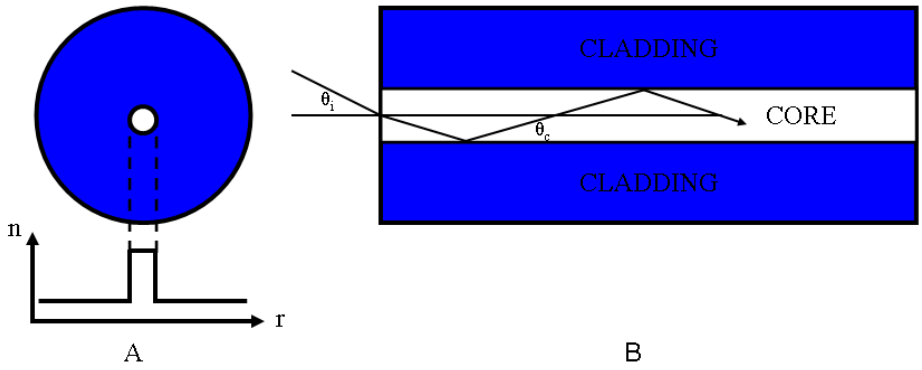

Fig 5.1. (A) Refractive index profile of a single mode optical fiber. The core (white) is concentrically oriented to the cladding (blue). (B) Schematic representation of total internal reflection. Incident light is bent towards the optical axis of the fiber and reflected off the core/cladding interface at angles equal or greater to the critical angle.

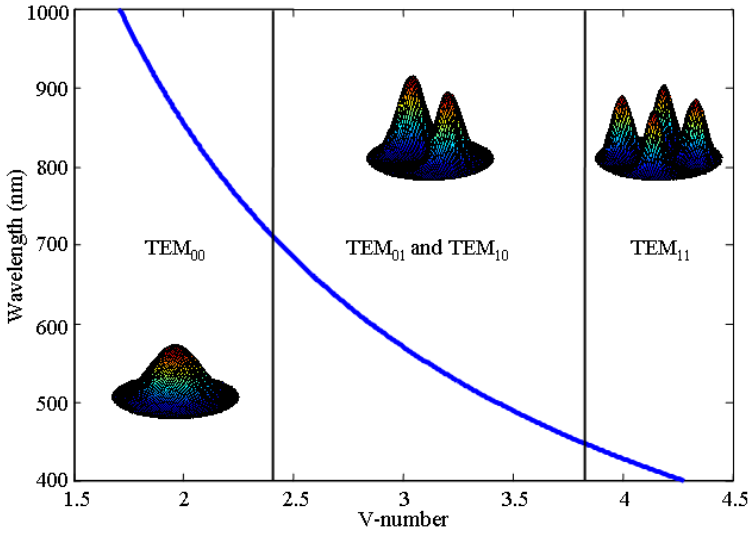

Fig. 5.2. Plot of wavelength vs. *V*-number. Vertical lines delineate mode cutoff regions. Within the mode regions are the spatial intensity profiles of the supported fiber modes.

In practice, the core diameter of single mode fiber (SMF) is less important than the guided mode field diameter (MFD). The MFD corresponds to the field diameter where the intensity is reduced by $1/e^2$ and is given as

$$w(\lambda) = 2a\left(.65 + \frac{1.619}{V^{3/2}} + \frac{2.879}{V^6}\right) \qquad (5.4)$$

Therefore, for maximum coupling efficiency of a Gaussian beam into a SMF the MFD and NA of the focused beam must match those of the optical fiber.

The guided mode confined to the core of the optical fiber has two orthogonal polarization vectors. Breaks in cylindrical symmetry and deviations in the circular shape of the core cause these polarization vectors to couple with one another as a beam propagates through the optical fiber. In order to prevent polarization mode coupling an elliptisity can be placed in the core or a stress birefringence in one plane of the core to prevent polarization mode coupling. In both cases the effective symmetry of the core is broken. This confines a polarization mode coupled parallel or perpendicular to the symmetry break to the aligned axis. Fiber designs for polarization maintaining fibers are illustrated in Fig. 5.3.

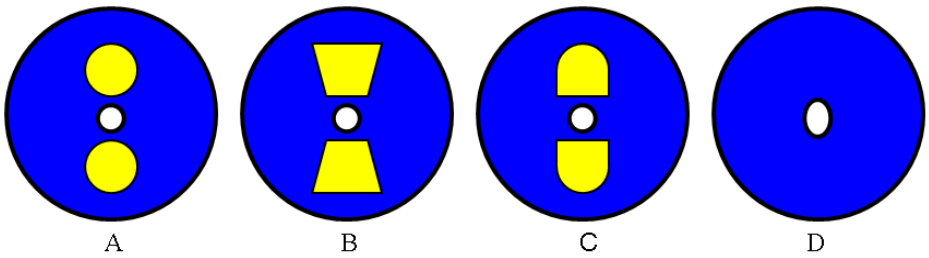

Fig. 5.3. Schematic representations of various polarization maintaining fiber designs. (A) PANDA (B) Bow-tie (C) D-type (D) Elliptical core. The slow axis for all fibers is oriented vertically with the page.

A new generation of optical fiber was introduced in the early 1990's that allow for a break in traditional optical fiber parameters. The first type, defined as microstructured fibers (MF's), have a pure silica glass core surrounded by an array of air holes within a pure silica cladding. Total internal reflection remains the mechanism of confinement, as the air holes reduce the effective refractive index of the cladding. Manipulation of the air filling fraction, core diameter and core shape allows optical fiber designers to manipulate dispersion, modal, nonlinear, and polarization properties of theses fibers. Such designs have allowed the creation of optical fibers with the zero dispersion point shifted to anywhere in the visible spectrum (zero dispersion of silica is ~1.3μm), optical

fibers with large core mode areas that maintain single mode operation across a spectrum of several hundred nanometers, and highly nonlinear fibers with core diameters much smaller than those possible with step-index designs. Additionally, MF's can be produced with a solid silica core surrounded by a holey cladding with few air holes of lower effective refractive index surrounded by a second cladding with large air holes of very low effective refractive index. This arrangement creates a "dual core" fiber which can be advantageous in an all optical fiber NLOM. MF's have lead to a renaissance in nonlinear fiber optics.

In some fiber designs the air holes in the cladding can be arranged to form a two-dimensional periodic array. Fibers designed in this manner are known as photonic crystal fibers (PCF's). A sub category of PCF's have hollow air cores surrounded by a photonic crystal cladding and are referred to as hollow-core photonic crystal fibers (HC-PCF's) or photonic bandgap fibers. In HC-PCF's light is confined to the core by the periodic variations of the refractive index in the photonic crystal cladding. These periodic structures invoke a photonic bandgap effect identical in nature to the bandgap between electronic energy levels. The periodic arrangement of airholes in the cladding creates a crystalline structure with a defined set of allowed propagation frequencies. The crystalline structure dictates that disallowed frequencies will be confined to a central (core) defect. The reduced nonlinearity coefficient of the air core and zero dispersion point being located in the middle of the bandgap has made this class of optical fiber popular for ultrashort pulse transmission. Other nonlinear effects can be exploited by filling the hollow core with a gas or liquid[106].

5.2 OPTICAL FIBER DELIVERY OF ULTRASHORT PULSES FOR NONLINEAROPTICAL MICROSCOPY*

Nonlinear optical microscopy (NLOM) utilizing femtosecond laser pulses is a proven

*Reprinted with permission from A. M. Larson and A. T. Yeh, "Delivery of sub-10-fs pulses for Nonlinear Optical Microscopy by Polarization-Maintaining Single Mode Optical Fiber," *Opt. Express* **16**, 14723-14730 (2008) ©Optical Society of America http://www.opticsinfobase.org/abstract.cfm?URI=oe-16-19-14723

tool for imaging living tissues[1]. However, further characterization of tissues in their native environment requires miniaturization of bench top microscopy systems into portable, optical fiber based imaging systems[29, 30]. Optical fiber pulse delivery systems[31-34] provide a simple and efficient platform on which to develop miniaturized microscopes[35-37] and microendoscopes[29, 38, 39] for tissue interrogation without excision. A difficult challenge in developing these imaging systems is preserving the temporal and spectral characteristics of femtosecond laser pulses at the focal plane. The susceptibility of ~100 fs pulses, common in current systems, to severe nonlinear broadening limits pulse energies delivered to the specimen of tens of picojoules or requires complex optical systems to control. Here, we report the optical fiber delivery of high energy (≥1 nJ), dispersion minimized sub-10-fs pulses to NLOM focus for imaging using simple dispersion compensation.

Femtosecond pulse propagation through single mode optical fiber (SMF) is governed by the interplay of linear (dispersion) and nonlinear (i.e., self-phase modulation, SPM) effects[107] arising within the core. Group velocity dispersion (GVD) will broaden the pulse over a characteristic length (factor of 1.4 for Gaussian pulses) given by, $L_D = \frac{T_o^2}{|\beta_2|}$, where T_o and β_2 (40 ps^2/km) are the laser (transform-limited) pulse duration and GVD coefficient, respectively. It is estimated that $L_D < 3$ mm in SMF for a sub-10-fs pulse. Nonlinearities in SMF will similarly broaden the pulse by SPM over a nonlinear interaction length, $L_{NL} = \frac{1}{\gamma P_o}$, where P_o and γ (5 W^{-1}km^{-1}) are the input peak power and SMF nonlinearity coefficient, respectively. For 1 nJ pulse energy, significant pulse broadening is estimated to occur within a few millimeters for a sub-10-fs pulse. The ratio, $L_D / L_{NL} \approx 1$, indicates that nonlinear pulse propagation is mitigated by dispersion mediated pulse broadening, and hence, peak intensity reduction, occurring on the same length scale.

Fiber nonlinear effects have been minimized by either manipulating fiber properties or pulse shaping methods. Large mode area fibers have been used to decrease, but not eliminate, nonlinearity[31, 33, 108]. A novel high dispersion, few mode fiber has been developed where the dispersion interaction length is sufficiently shorter than the nonlinear interaction length allowing dispersion dominated pulse propagation for 150 fs pulses at 1 nJ[109]. Reconstruction of 100 fs pulses following sequential propagation through two SMFs has been demonstrated. Self-phase modulation in the first SMF spectrally (and temporally) broadened the pulse. A negatively dispersive element compensated for normal dispersion in both fibers and SPM of pulses with negative group delay dispersion (GDD) in the second SMF narrowed the pulse spectrum resulting in pulses of the same duration as the input[110]. Coherent pulse shaping methods[111, 112] relying on spatial light modulators have been used to compensate for nonlinear pulse distortion, however, high system losses limit power within the fiber. Highly chirped 50 fs pulses[113] have been delivered through short pieces of SMF at moderate power levels, although, significant post fiber normal dispersion was required and spectral narrowing was still observed.

Hollow-core photonic crystal fibers (HC-PCF's) have allowed the distortion free delivery of 100 fs pulses[52] propagating at and near the zero dispersion wavelength of the fiber. The steep dispersion slope, limited bandgap (~60-80 nm), and zero dispersion wavelength in the middle of the bandgap make these fibers unsuitable for broadband pulse propagation. Additionally, 100 fs pulse systems relying on HC-PCF's require adjustment of dispersion compensation for each new central wavelength, which is critical for fiber lengths longer than a few centimeters. This complicates the imaging of samples labeled with multiple fluorophores that do not have well overlapping excitation spectra.

A common method to deliver pulses with net-zero GDD to the focus of an optical fiber based NLOM is to pre-compensate normal dispersion from the SMF and downstream microscopy optics with negative GDD. Following the SMF, the remaining negative GDD necessary to compensate dispersion of strong focusing optics is

approximately 1,000 fs^2. The peak intensity of 100 fs pulses having 1,000 fs^2 GDD is reduced by <4%, and is not sufficient to reduce fiber nonlinearity. This is consistent with previous observations of nonlinear propagation of 100 fs pulses in optical fiber causing spectral narrowing of the pulse and a corresponding increase in pulse duration detrimental to efficient optical signal generation for NLOM. In contrast, this amount of GDD reduces peak intensity of sub-10-fs pulses by a factor ≥25, suggesting dispersion dominated propagation through SMF in microscopy applications. The high susceptibility of sub-10-fs pulses to dispersion will mitigate nonlinearity in optical fiber delivery at pulse energies in excess of 1nJ without relying on expensive, exotic waveguides or complex optical systems. Furthermore, the broad pulse spectrum of the delivered ultrashort laser pulse may be used for multiple fluorophore excitation without laser tuning and for efficient signal generation. Our system represents a significant improvement over those previously reported in terms of simplicity and reduced cost while increasing imaging efficiency and versatility.

5.2.1 PMF Delivery of Femtosecond Pulses

In our design, sub-10-fs pulses originating from a Ti:Al_2O_3 oscillator (Femtosource, Femtolasers) were stretched to ~8.5 ps (~22,000 fs^2 negative GDD) using three pairs of dispersion compensation mirrors (Femtolasers) before being coupled into ~400 mm of bare PMF (PM780 HP, Nufern). Normal dispersion of the PMF temporally recompressed the pulse to ~1.5 ps. The peak intensity of a 1 nJ pulse broadened to 1.5 ps in duration was not sufficient ($L_D / L_{NL} \approx .008$) to produce nonlinear pulse broadening within the PMF. Final recompression occurred while passing through the optics of the NLOM (~4000 fs^2) to deliver net zero GDD at the focal plane, schematically illustrated in Fig. 5.4. An achromatic zero-order $\lambda/2$ wave plate was used to align the laser polarization with an axis of the PMF. A near-infrared corrected achromat was used to couple the pulses (2 nJ) into PMF with ~50% efficiency. Fiber length was limited by the

amount of negative GDD imparted by the dispersion compensation mirrors and throughput efficiency of the optical system.

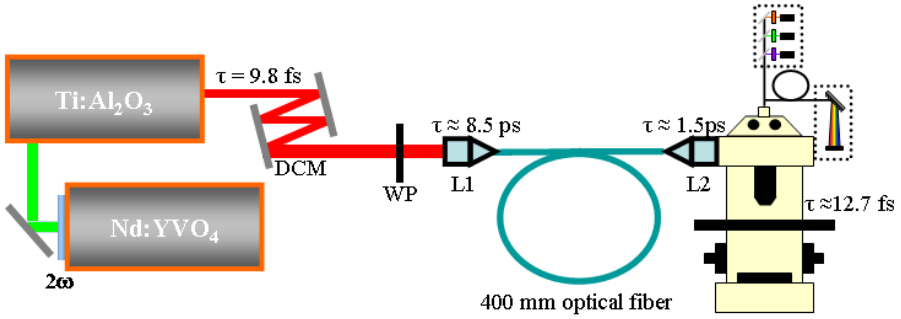

Fig. 5.4. Basic schematic diagram for optical fiber delivery sub-10-fs pulses. Pulses were stretched using dispersion compensation mirrors (DCM). Polarization was aligned to a fiber axis using a λ/2 waveplate (WP). Coupling lens (L1) focuses the beam into the PMF and is collimated by lens (L2). Pulses were directed into the microscope and signals were detected using photomultiplier tubes or a fiber coupled spectrometer.

Pulse spectra preceding and following the PMF, shown in Fig. 5.5(A), were measured by inserting a portable spectrometer (USB2000, Ocean Optics) into the beam path following the fiber collimating lens. The post fiber spectrum exhibited a modulated structure that most likely resulted from modal interference from the elliptical beam. Signal generated in a GaAsP (two-photon) photodiode was measured with respect to PMF laser input energy and exhibited a quadratic dependence indicating linear pulse propagation through the fiber as shown in Fig. 5.5(B). The modulations in the pulse spectrum remained with <60pJ coupled into the PMF. These same characteristics were observed when using isotropic (non-polarization maintaining) SMF.

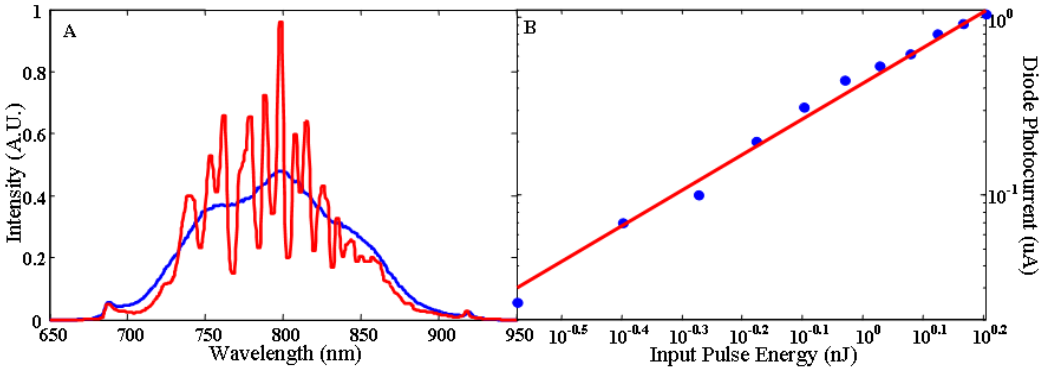

Fig. 5.5. (A) Pulse spectra normalized to energy directly from the oscillator (blue) and after propagation through PMF (red). (B) Logarithmic plot of measured photocurrent from a GaAsP photodiode as a function of laser power into PMF (blue circles). Quadratic fit to data points shown for reference (red line).

5.2.2 Femtosecond Pulse Characterization for Nonlinear Optical Microscopy

Pulse duration was measured by interferometric autocorrelation at the focal plane of the NLOM imaging system. An interferometric autocorrelation of the pulse delivered through PMF at the NLOM focal plane is shown in Fig. 5.6(A). The collimated beam was directed through a Michelson interferometer with collinear beams steered to the microscope passing through a 1.5X telescope and reflected off the primary dichroic mirror (635dcspxruv3p, Chroma) to a Zeiss 40X Achroplan (0.8NA) water immersion objective. The objective focused the beam through a water column onto a GaAsP photodiode[88] with a 1 mm thick borosilicate window. Fine dispersion control was provided by inserting BK7 glass windows (1 mm thickness increments) into the beam path after the fiber.

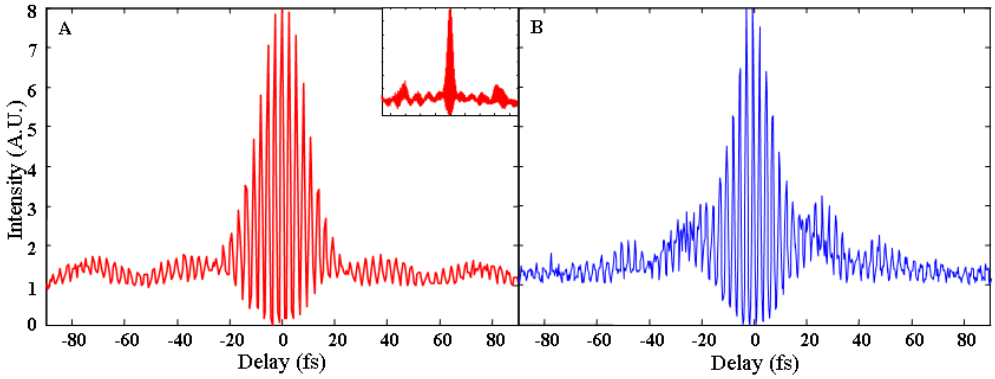

Fig. 5.6. Interferometric autocorrelation of fiber (A) and air (B) delivered pulses taken at the NLOM focal plane. Inset (A) Autocorrelation with long delays.

The measured pulse duration of 12.7 fs was calculated from the central peak FWHM assuming a sech^2 pulse shape. Oscillations at long delays of the autocorrelation were the result of residual chirp and modulations in the post fiber pulse spectrum, see inset Fig. 5.6(A). The width of the central peak was identical to a previous measurement for this objective[9], shown in Fig. 5.6(B), suggesting optimal dispersion management through PMF. Estimates of $\beta_2 = 40$ fs^2/mm and $\beta_3 = 30$ fs^3/mm (third-order dispersion, TOD) for PMF were based on our measurements and $\beta_3/\beta_2 \approx 0.75$ for silica. TOD mismatch in the fiber arose from TOD/GDD $\approx$ 0.68 for our dispersion compensation mirrors. Noticeably absent from the autocorrelation in Fig. 5.6(A) were side lobes resulting from chromatic and spherical aberration of the objective lens as observed in Fig. 5.5(B)[9]. Side lobes were not present in Fig. 5.6(A) because the final beam diameter filled 35% of the back focal aperture compared to 70% without the fiber to minimize beam clipping in the interferometer. It should be noted that the effects of spherical aberration, chromatic aberration and a radially dependent dispersion profile of the objective ultimately limit the pulse duration at the sample. Minimizing these effects requires well corrected objective lenses for good pulse maintenance making the now common practice of using gradient index (GRIN) objectives for in-vivo nonlinear microscopic imaging incompatible with laser pulses of such short duration.

Imaging performance was measured by comparing two-photon excited fluorescence (TPF) of three common biological fluorophores Indo-1 (Molecular Probes), FITC (Sigma) and TRITC (Sigma), and image analysis of second harmonic generation (SHG) in collagen from rat skin. Fluorescent dyes were dissolved in their appropriate solvents to a concentration of 100 μM. TPF was generated by focusing laser pulses into individual dye solutions using the 40X Achroplan objective and detected in the backscattered direction by the focusing objective. Fluorescence signal was coupled, non-descanned, into a multimode optical fiber connected to a spectrometer (SpectraPro 2300i, Roper Scientific) shown in Fig. 5.4. Back scattered laser light was filtered using 3 mm BG-39 glass. Relative excitation efficiency was determined by comparing the emission intensity from each dye excited with the laser delivered through air and by the PMF. A longer focal length collimating lens for the fiber was used to ensure matched objective NA.

Non-resonant two-photon excitation by femtosecond pulses can be understood by examining the two-photon excitation power spectrum[70, 71],

$$T(\omega) = \left| \int_0^\infty E\left(\omega/2 + \Omega\right) E\left(\omega/2 - \Omega\right) d\Omega \right|^2, \qquad (5.5)$$

where $E(\omega)$ is the Fourier transform of electric field $E(t)$ and Ω is an iterative variable that ensures integration over non-degenerate (sum frequency) and degenerate (second harmonic) frequency combinations. Assuming transform limited pulses, calculated $T(\omega)$ using the laser and post fiber spectrum are shown in Fig. 5.7(A). The probability of non-resonant two-photon absorption is proportional to the overlap integral[72, 73],

$$\Gamma \propto \int_{-\infty}^{\infty} \sigma^{(2)}(\omega) T(\omega) d\omega, \qquad (5.6)$$

where $\sigma^{(2)}(\omega)$ is the molecular two-photon absorption profile. $\sigma^{(2)}(\omega)$ for the three dyes was estimated by measuring TPF intensity as a function of central wavelength (two-photon photoluminescence excitation spectrum) of a narrowband, 170 fs Ti:Al_2O_3 laser (Mira 900F, Coherent). It was assumed that $\sigma(\omega)$ of the dyes was directly proportional with their two-photon photoluminescence excitation spectra and are shown in Fig.

5.6(B). The laser $T(\omega)$ is shown for reference and indicates that our broadband pulse was well suited to excite the different fluorophores simultaneously.

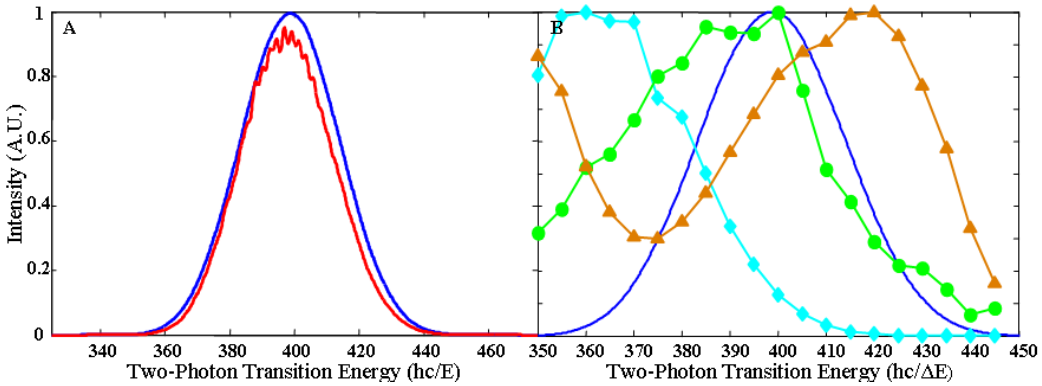

Fig 5.7. (A) Calculated T(ω) of the laser (blue) and PMF pulse spectra (red). (B) Two-photon photoluminescence excitation spectra for Indo-1 (diamond, cyan), FITC (circle, green), and TRITC (triangle, orange), Calculated T(ω) of the laser pulse shown for reference (solid line, blue).

PMF, with respect to air, delivered pulses generated TPF from individual Indo-1, FITC and TRITC solutions to within 43.7%, 42.2% and 36.0%, respectively. Using Equation 5.6, it was calculated PMF delivered pulses should generate TPF signal within 10.4%, 10.1% and 13.5% for Indo-1, FITC and TRITC, respectively, compared to air delivered pulses. The measured and calculated TPF comparisons were brought into closer agreement by including residual chirp in the PMF delivered pulse of <30 fs^2 (~.8 mm fused silica) and 1,200 fs^3 (estimated TOD mismatch). This calculation does not take into account focal volume differences from slightly different degrees of collimation of the incident beams. All three dyes were combined and their simultaneous TPF emission profiles are shown in Fig. 5.8 excited using PMF and air delivered pulses. TPF emission spectra were normalized to the TRITC emission peak. The TPF spectra indicate a disproportionate decrease in the high energy side of the PMF delivered two-photon excitation power spectrum more than likely resulting from (additional) residual chirp in the pulse.

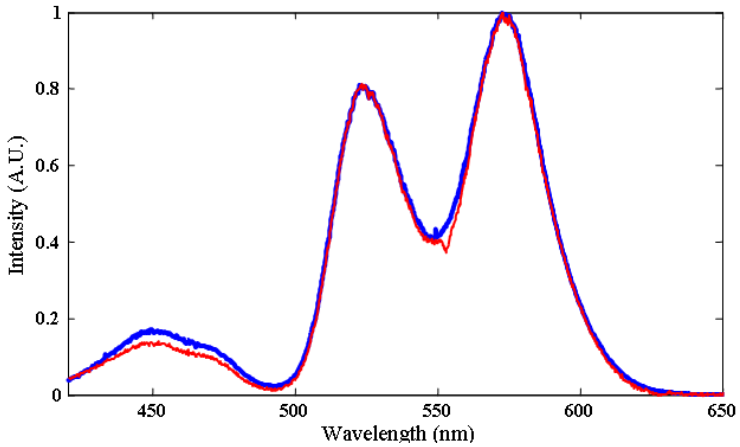

Fig. 5.8. Simultaneous excitation of Indo-1, FITC and TRITC using laser pulses delivered through air (blue) and PMF (red).

NLOM images of rat skin using SHG in collagen are shown in Fig. 5.9 obtained with air (A) and PMF delivered pulses (B and C). Skin was excised from recently sacrificed 6 week old Sprague-Dawley rats. NLOM images were acquired at 0.0625 Hz frame rate and averaged over four frames from the dermal side at a depth of 15μm. SHG signal is collected in the backscattered direction and directed non-descanned onto a PMT depicted in Fig. 5.4. A 430dcxru long pass dichroic mirror (Chroma) and HQ405/40 bandpass filter (Chroma) are placed in front of the PMT. Intensity analysis was performed by averaging pixel intensity over each set of images. The incident laser polarization orientations are indicated by double-headed arrows. The images were from the same focal plane and showed similar collagen morphology and resolution. Intensity analysis of NLOM images indicated PMF delivered pulses were capable of generating second harmonic signals to within a factor of 2 to 3. The measured polarization extinction ratio of the laser following PMF was 170:1 compared to 500:1 for the oscillator. A dominant uniaxial component of collagen second-order susceptibility has been measured aligned along the fiber axis[114]. From Fig. 5.8(B) to (C), the incident polarization was rotated 90° to demonstrate spectroscopic contrast was maintained with PMF delivered pulses. It was observed that fibers aligned along the incident polarization were preferentially highlighted in the SHG images.

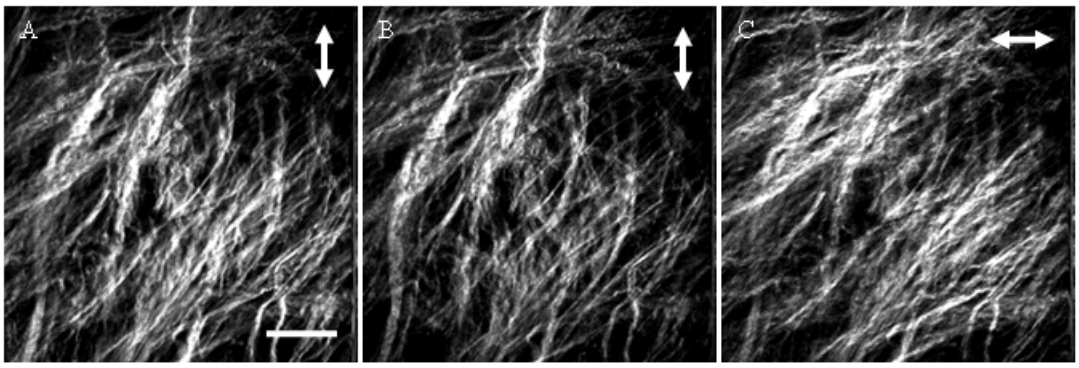

Fig. 5.9. NLOM images of collagen fibers in rat skin using second harmonic generation with air (A) and fiber (B-C) delivered pulses. Double headed arrows indicate direction of incident laser polarization. Image depth is 15μm. Scale bar is 20 μm.

5.3 CONCLUDING REMARKS

We have demonstrated sub-10-fs pulses can be delivered via 400 mm of PMF to the focus of an NLOM system with minimal spectral and temporal distortion. Our data suggest that longer PMF lengths can be used with proportional addition of dispersion compensation (cf. Fig. 5.4(B)). Nonlinear optical signal generation, particularly TPF and SHG, by PMF delivered pulses was shown to be within a factor of 2 to 3 of air delivered pulses. The bandwidth of PMF delivered pulses was sufficiently wide to excite multiple fluorophores simultaneously eliminating the need for central wavelength tuning and concomitant adjustments in dispersion compensation. Furthermore, polarization was maintained providing an additional mechanism of image contrast for optical fiber based NLOM. Our design provides a simple, efficient, and experimentally flexible platform to develop miniaturized nonlinear microscopy and microendoscopy imaging systems motivated by *in vivo* multi-molecular imaging studies in small animals.

CHAPTER VI
CONCLUSIONS AND FUTURE WORK

This body of research focused on the development and characterization of an optical fiber based multispectral NLOM. The novelty of the work lies in the use of sub-10-fs pulses for nonlinear optical signal generation. Throughout this dissertation we have shown that sub-10-fs pulses can be delivered to the focal plane of the NLOM with minimal changes to the time-bandwidth product. The ability to deliver ultrashort pulses allows for the simultaneous excitation of multiple fluorophores. This has been exploited in a multispectral imaging application using an *in-vivo* angiogenesis model. We have also demonstrated the ability to deliver ultrashort pulses through polarization-maintaining single mode optical fiber. Data presented in this work can serve as the basis for further development of an all optical fiber based NLOM for the interrogation of large and intact specimen. Our results also indicate pulses of even shorter duration can be used in NLOM.

The use of sub-10-fs pulses in NLOM requires characterizing the effects of the optical system on the pulses. Temporal distortions imparted by the NLOM were compensated using dispersion compensating (chirped) mirrors. Measurement of the laser pulse width at the focal plane of the NLOM guarantees the reduction in phase distortion imparted by the optical system and the pulse distortion imparted by aberration in the optical system that can not be compensated. A biological sample (mouse tail tendon) was used to measure laser pulse duration in an effort to evaluate the effects of common tissue constituents (collagen) on nonlinear signal generation. The ability to measure sub-13-fs pulse durations in mouse tail tendon at the focus of the NLOM indicates the entire pulse spectrum is available to extracellular matrix constituents for second harmonic generation and fluorescent probes in two-photon absorption. Reconstruction of the pulse in the sample maximized nonlinear optical signals allowing the collection of high signal to noise ratio images.

In NLOM applications, the short pulse duration and broad spectral bandwidth of the laser pulses emitted from our oscillator hold several advantages. Primarily, the increased peak power of the pulse allows a reduction in average power applied to the sample which limits thermal damage. Furthermore, the susceptibility of sub-10-fs pulses to temporal broadening may limit out of focus fluorescence generated when using high energy pulses for deep tissue imaging. This can improve the signal to noise ratio of the images and may lead to an enhancement in the depth penetration ability of NLOM. The reduction in temporal duration of a laser pulse necessarily leads to an increase in spectral content. We have shown that the broad (~125 nm) bandwidth of sub-10-fs pulses can be used to simultaneously excite multiple fluorescent probes without the need to tune the laser and rescan the sample. In this work we have demonstrated the excitation of fluorophores and fluorescent proteins whose absorption spectra are well separated. Eliminating the need for laser tuning for efficient nonlinear signal generation in multiple fluorescent probes further reduces the thermal and photodamage incurred while scanning the sample multiple times.

The ability to generate signal from multiple endogenous and exogenous fluorescent probes simultaneously requires the proper discrimination of the detected signals. To this extent, multispectral imaging is invaluable. Spectral detection capabilities allow for the pixel by pixel segmentation of all detected signal constituents. A full spectrum is acquired for each pixel in the image which spatially segregates the contrast mechanisms. Pixels in the image can then be displayed using their corresponding spectral content. Multispectral imaging can open many new avenues for the investigation of cell-cell, cell-extracellular matrix interactions and genetic profiling.

We have also demonstrated the ability to deliver sub-10-fs pulses to the NLOM via 400 mm of polarization-maintaining single mode optical fiber. Great efforts have been made to eliminate the detrimental nonlinear effects that occur when focusing intense femtosecond pulses into the narrow core of a single mode optical fiber. Nonlinear effects have been overcome by relying on the high susceptibility of sub-10-fs pulses to dispersion mediated pulse broadening. We have used dispersion compensating mirrors

to impart negative group delay dispersion equal to the positive group delay dispersion of the optical fiber, associated coupling optics and the NLOM. The residual chirp remaining on the pulse at the fiber exit sufficiently reduces the peak power within the optical fiber negating nonlinear effects. The limit on fiber length using our system is the amount of negative dispersion that can be imparted on the pulse and the power losses associated with beam steering and dispersion compensation. Our technique allows the delivery of laser pulses of equal temporal duration through optical fiber or air to the NLOM. Fiber delivered pulses are capable of generating detectable signals within a factor of three of pulses delivered through air.

The delivery of sub-10-fs pulses via optical fiber is a necessary developmental step in creating a NLOM with multiple degrees of freedom. A future imaging system will have the ability to pivot around all three axes and not be designed around an upright or inverted light microscope. This will allow for the interrogation of large and intact specimen that can not fit on the stage of a conventional microscope. Optical fiber transmission of excitation laser light and detected nonlinear signals removes translation and realignment constraints imposed by a fixed beam path. Additionally, it is possible to use laser pulses having shorter temporal duration than those used in this work with dispersion compensating optics having sufficient bandwidth. The increased spectral content of shorter duration pulses will benefit higher energy pulse delivery through the optical fiber.

REFERENCES

1. A. T. Yeh, H. Gibbs, J.-J. Hu, and A. M. Larson, "Advances in nonlinear optical microscopy for visualizing dynamic tissue properties in culture," Tissue Eng. B Rev. **14**, 119-131 (2008).

2. W. Denk, J. H. Strickler, and W. W. Webb, "Two-photon laser scanning fluorescence microscopy," Science **248**, 73-76 (1990).

3. W. R. Zipfel, R. M. Williams, and W. W. Webb, "Nonlinear magic: multiphoton microscopy in the biosciences," Nat. Biotechnol. **21**, 1369-1377 (2003).

4. P. J. Campagnola, and L. M. Loew, "Second-harmonic imaging microscopy for visualizing biomolecular arrays in cells, tissues and organisms," Nat. Biotechnol. **21**, 1356-1360 (2003).

5. P. Theer, M. T. Hasan, and W. Denk, "Two-photon imaging to a depth of 1000um in living brains by use of a Ti:Al_2O_3 regenerative amplifier," Opt. Lett. **28**, 1022-1024 (2003).

6. G. McConnell, and E. Riis, "Two-photon laser scanning fluorescence microscopy using photonic crystal fiber," J. Biomed. Opt. **9**, 922-927 (2004).

7. G. McConnell, "Improving the penetration depth in multiphoton excitation laser scanning microscopy," J. Biomed. Opt. **11**, 054020 (2006).

8. S. Tang, T. B. Krasieva, Z. Chen, G. Tempea, and B. J. Tromberg, "Effect of pulse duration on two-photon excited fluorescence and second harmonic generation in nonlinear optical microscopy," J. Biomed. Opt. **11**, 0205011-0205013 (2006).

9. A. M. Larson, and A. T. Yeh, "*Ex vivo* characterization of sub-10-fs pulses," Opt. Lett. **31**, 1681-1683 (2006).

10. W. Du, Y. Wang, Q. Luo, and B. F. Liu, "Optical molecular imaging for systems biology: from molecule to organism," Anal. Bioanal. Chem. **386**, 444-457 (2006).

11. C. E. Fuller, H. Wang, W. Zhang, G. N. Fuller, and A. Perry, "High-throughput molecular profiling of high-grade astrocytomas: the utility of fluorescence *in situ* hybridization on tissue microarrays (TMA-FISH)," J. Neuropathol. Exp. Neurol. **61**, 1078-1084 (2002).

12. S. Gross, and D. Piwnica-Worms, "Spying on cancer: molecular imaging *in vivo* with genetically encoded reporters," Cancer cell **7**, 5-15 (2005).

13. S. Kumar, and R. Richards-Kortum, "Optical molecular imaging agents for cancer diagnostics and therapeutics," Nanomed. **1**, 23-30 (2006).

14. X. Gao, and S. Nie, "Molecular profiling of single cells and tissue specimens with quantum dots," Trends. Biotechnol. **21**, 371-373 (2003).

15. P. Stoller, K. M. Reiser, P. M. Celliers, and A. M. Rubenchik, "Polarization-modulated second harmonic generation in collagen," Biophys. J. **82**, 3330-3342 (2002).

16. R. M. Williams, W. R. Zipfel, and W. W. Webb, "Interpreting second-harmonic generation images of collagen I fibrils," Biophys. J. **88**, 1377-1386 (2005).

17. P. J. Campagnola, M.-d. Wei, A. Lewis, and L. M. Loew, "High-resolution nonlinear optical imaging of live cells by second harmonic generation," Biophys. J. **77**, 3341-3349 (1999).

18. T. Boulesteix, E. Beaurepaire, M. P. Sauviat, and M. C. Schanne-Klein, "Second-harmonic microscopy of unstained living cardiac myocytes: measurements of sarcomere length with 20-nm accuracy," Opt. Lett. **29**, 2031-2033 (2004).

19. S. V. Plotnikov, A. C. Millard, P. J. Campagnola, and W. A. Mohler, "Characterization of the myosin-based source for second-harmonic generation from muscle sarcomeres," Biophys. J. **90**, 693-703 (2006).

20. D. W. Piston, B. R. Masters, and W. W. Webb, "Three-dimensionally resolved NAD(P)H cellular metabolic redox imaging of the *in situ* cornea with two-photon excitation laser scanning microscopy," J. Microsc. **178**, 20-27 (1995).

21. B. R. Masters, P. T. So, and E. Gratton, "Multiphoton excitation fluorescence microscopy and spectroscopy of *in vivo* human skin," Biophys. J. **72**, 2405-2412 (1997).

22. S. Huang, A. A. Heikal, and W. W. Webb, "Two-photon fluorescence spectroscopy and microscopy of NAD(P)H and flavoprotein," Biophys. J. **82**, 2811-2825 (2002).

23. J. V. Rocheleau, W. S. Head, and D. W. Piston, "Quantitative NAD(P)H/flavoprotein autofluorescence imaging reveals metabolic mechanisms of pancreatic islet pyruvate response," J. Biol. Chem. **279**, 31780-31787 (2004).

24. Y. Wu, and J. Y. Qu, "Two-photon autofluorescence spectroscopy and second-harmonic generation of epithelial tissue," Opt. Lett. **30**, 3045-3047 (2005).

25. A. Zoumi, A. Yeh, and B. J. Tromberg, "Imaging cells and extracellular matrix *in vivo* by using second-harmonic generation and two-photon excited fluorescence," Proc. Natl. Acad. Sci. U S A **99**, 11014-11019 (2002).

26. A. T. Yeh, N. Nassif, A. Zoumi, and B. J. Tromberg, "Selective corneal imaging using combined second-harmonic generation and two-photon excited fluorescence," Opt. Lett. **27**, 2082-2084 (2002).

27. K. Konig, "Multiphoton microscopy in life sciences," J. Microsc. **200**, 83-104 (2000).

28. K. Konig, K. Schenke-Layland, I. Riemann, and U. A. Stock, "Multiphoton autofluorescence imaging of intratissue elastic fibers," Biomaterials **26**, 495-500 (2005).

29. B. A. Flusberg, J. C. Jung, E. D. Cocker, E. P. Anderson, and M. J. Schnitzer, "*In vivo* brain imaging using a portable 3.9 gram two-photon fluorescence microendoscope," Opt. Lett. **30**, 2272-2274 (2005).

30. L. Fu, and M. Gu, "Fibre-optic nonlinear optical microscopy and endoscopy," J. Microsc. **226**, 195-206 (2007).

31. F. Helmchen, D. W. Tank, and W. Denk, "Enhanced two-photon excitation through optical fiber by single-mode propagation in a large core," Appl. Opt. **41**, 2930-2934 (2002).

32. S.-P. Tai, M.-C. Chan, T.-H. Tsai, S.-H. Guol, L.-J. Chen, and C.-K. Sun, "Two-photon fluorescence microscope with a hollow-core photonic crystal fiber," Opt. Express **12**, 6122-6128 (2004).

33. M.-C. Chan, T.-M. Liu, S.-P. Tai, and C.-K. Sun, "Compact fiber-delivered Cr:forsterite laser for nonlinear light microscopy," J. Biomed. Opt. **10**, 0540061-0540064 (2005).

34. L. Fu, X. Gan, and M. Gu, "Nonlinear optical microscopy based on double-clad photonic crystal fibers," Opt. Express **13**, 5528-5534 (2005).

35. F. Helmchen, M. S. Fee, D. W. Tank, and W. Denk, "A miniature head-mounted two-photon microscope: high resolution brain imaging in freely moving animals," Neuron **31**, 903-912 (2001).

36. W. Gobel, J. N. D. Kerr, A. Nimmerjahn, and F. Helmchen, "Miniaturized two-photon microscope based on a flexible coherent fiber bundle and a gradient-index lens objective," Opt. Lett. **29**, 2521-2523 (2004).

37. C. J. Engelbrecht, R. S. Johnston, E. J. Seibel, and F. Helmchen, "Ultra-compact fiber-optic two-photon microscope for functional fluorescence imaging *in vivo*," Opt. Express **16**, 5556-5564 (2008).

38. L. Fu, A. Jain, H. Xie, C. Cranfield, and M. Gu, "Nonlinear optical endoscopy based on a double-clad photonic crystal fiber and a MEMS mirrors," Opt. Express **14**, 1027-1032 (2006).

39. M. T. Myaing, D. J. MacDonald, and X. Li, "Fiber-optic scanning two-photon fluorescence endoscope," Opt. Lett. **31**, 1076-1078 (2006).

40. H. Bao, J. Allen, R. Pattie, R. Vance, and M. Gu, "Fast handheld two-photon fluorescence microendoscope with a 475 microm x 475 microm field of view for *in vivo* imaging," Opt. Lett. **33**, 1333-1335 (2008).

41. P. Anikijenko, L. T. Vo, E. R. Murr, J. Carrasco, W. J. McLaren, Q. Chen, S. G. Thomas, P. M. Delaney, and R. G. King, "*In vivo* detection of small subsurface melanomas in athymic mice using noninvasive fiber optic confocal imaging," J. Invest. Dermatol. **117**, 1442-1448 (2001).

42. L. D. Swindle, S. G. Thomas, M. Freeman, and P. M. Delaney, "View of normal human skin *in vivo* as observed using fluorescent fiber-optic confocal microscopic imaging," J. Invest. Dermatol. **121**, 706-712 (2003).

43. A. P. Wells, L. Wakely, W. Birchall, and P. M. Delaney, "*In vivo* fibreoptic confocal imaging (FOCI) of the human ocular surface," J. Anat. **208**, 197-203 (2006).

44. T. Ota, H. Fukuyama, Y. Ishihara, H. Tanaka, and T. Takamatsu, "*In situ* fluorescence imaging of organs through compact scanning head for confocal laser microscopy," J. Biomed. Opt. **10**, 024010 (2005).

45. R. Kiesslich, J. Burg, M. Vieth, J. Gnaendiger, M. Enders, P. Delaney, A. Polglase, W. McLaren, D. Janell, S. Thomas, B. Nafe, P. R. Galle, and M. F. Neurath, "Confocal laser endoscopy for diagnosing intraepithelial neoplasias and colorectal cancer *in vivo*," Gastroenterology **127**, 706-713 (2004).

46. R. Kiesslich, M. Goetz, M. Vieth, P. R. Galle, and M. F. Neurath, "Technology insight: confocal laser endoscopy for *in vivo* diagnosis of colorectal cancer," Nat. Clin. Pract. Oncol. **4**, 480-490 (2007).

47. K. C. Maitland, A. M. Gillenwater, M. D. Williams, A. K. El-Naggar, M. R. Descour, and R. R. Richards-Kortum, "*In vivo* imaging of oral neoplasia using a miniaturized fiber optic confocal reflectance microscope," Oral Oncol. (2008).

48. K. B. Sung, C. Liang, M. Descour, T. Collier, M. Follen, and R. Richards-Kortum, "Fiber-optic confocal reflectance microscope with miniature objective for *in vivo* imaging of human tissues," IEEE transactions on bio-medical engineering **49**, 1168-1172 (2002).

49. L. B. Boyette, M. A. Reardon, A. J. Mirelman, T. D. Kirkley, J. J. Lysiak, J. B. Tuttle, and W. D. Steers, "Fiberoptic imaging of cavernous nerves *in vivo*," J. Urol. **178**, 2694-2700 (2007).

50. R. A. Drezek, R. Richards-Kortum, M. A. Brewer, M. S. Feld, C. Pitris, A. Ferenczy, M. L. Faupel, and M. Follen, "Optical imaging of the cervix," Cancer **98**, 2015-2027 (2003).

51. R. F. Cregan, B. J. Mangan, J. C. Knight, T. A. Birks, P. S. Russell, P. J. Roberts, and D. C. Allan, "Single-mode photonic band gap guidance of light in air," Science **285**, 1537-1539 (1999).

52. W. Gobel, A. Nimmerjahn, and F. Helmchen, "Distortion-free delivery of nanojoule femtosecond pulses from a Ti:sapphire laser through a hollow-core photonic crystal fiber," Opt. Lett. **29**, 1285-1287 (2004).

53. J. Squier, and M. Muller, "High resolution nonlinear microscopy: A review of sources and methods for achieving optimal imaging," Rev. Sci. Instrum. **72**, 2855-2867 (2001).

54. P. W. Milonni, and J. H. Eberly, *Lasers* (John Wiley & Sons, New York, 1988).

55. D. H. Sutter, G. Steinmeyer, L. Gallmann, N. Matuschek, F. Morier-Genoud, U. Keller, V. Scheuer, G. Angelow, and T. Tschudi, "Semiconductor saturable-absorber mirror assisted Kerr-lens mode-locked Ti:sapphire laser producing pulses in the two-cycle regime," Opt. Lett. **24**, 631-633 (1999).

56. U. Morgner, F. X. Kartner, S. H. Cho, Y. Chen, H. A. Haus, J. G. Fujimoto, E. P. Ippen, V. Scheuer, G. Angelow, and T. Tschudi, "Sub-two-cycle pulses from a Kerr-lens mode-locked Ti:sapphire laser," Opt. Lett. **24**, 411-413 (1999).

57. R. Ell, U. Morgner, F. X. Kartner, J. G. Fujimoto, E. P. Ippen, V. Scheuer, G. Angelow, T. Tschudi, M. J. Lederer, A. Boiko, and B. Luther-Davies, "Generation of 5-fs pulses and octave-spanning spectra directly from a Ti:sapphire laser," Opt. Lett. **26**, 373-375 (2001).

58. T. Brabec, C. Spielmann, P. F. Curley, and F. Krausz, "Kerr lens mode locking," Opt. Lett. **17**, 1292-1294 (1992).

59. R. Paschotta, and U. Keller, "Ultrafast Solid-State Lasers " in *Ultrafast Lasers Technology and Applications*, M. E. Fermann, A. Galvanauskas, and G. Sucha, eds. (Marcel Dekker, Inc., New York, 2003).

60. L. Xu, G. Tempea, A. Poppe, M. Lezner, C. Spielmann, F. Krausz, A. Stingle, and K. Ferencz, "High-power sub-10-fs Ti:sapphire oscillators," Appl. Phys. B **65**, 151-159 (1997).

61. R. W. Boyd, *Nonlinear Optics* (Elsevier, Boston, 2008).

62. M. Goppert-Mayer, "Über elementarakte mit zwei quantensprüngen," Ann. Phys. **401**, 273-294 (1931).

63. W. Kaiser, and C. G. B. Garrett, "Two-photon excitation in CaF_2:Eu^{2+}," Phys. Rev. Lett. **7**, 229-231 (1961).

64. W. L. Peticolas, J. P. Goldsborough, and K. E. Rieckhoff, "Double photon excitation in organic crystals," Phys. Rev. Lett. **10**, 43-45 (1963).

65. W. L. Peticolas, and K. E. Rieckhoff, "Double-photon excitation of organic molecules in dilute solution," J. Chem. Phys. **39**, 1347-1348 (1963).

66. K. Konig, T. W. Becker, P. Fischer, I. Riemann, and K. J. Halbhuber, "Pulse-length dependence of cellular response to intense near-infrared laser pulses in multiphoton microscopes," Opt. Lett. **24**, 113-115 (1999).

67. J. M. Squirrell, D. L. Wokosin, J. G. White, and B. D. Bavister, "Long-term two-photon fluorescence imaging of mammalian embryos without compromising viability," Nat. Biotechnol. **17**, 763-767 (1999).

68. H. J. Koester, D. Baur, R. Uhl, and S. W. Hell, "Ca2+ fluorescence imaging with pico- and femtosecond two-photon excitation: signal and photodamage," Biophys. J. **77**, 2226-2236 (1999).

69. A. Hopt, and E. Neher, "Highly nonlinear photodamage in two-photon fluorescence microscopy," Biophys. J. **80**, 2029-2036 (2001).

70. D. Meshulach, and Y. Silberberg, "Coherent quantum control of two-photon transitions by a femtosecond laser pulse," Nature **396**, 239-242 (1998).

71. J. P. Ogilvie, K. J. Kubarych, A. Alexandrou, and M. Joffre, "Fourier transform measurement of two-photon excitation spectra: applications to microscopy and optimal control," Opt. Lett. **30**, 911-913 (2005).

72. D. Meshulach, and Y. Silberberg, "Coherent quantum control of multiphoton transitions by shaped ultrashort optical pulses," Phys. Rev. A. **60**, 1287-1292 (1999).

73. K. A. Walowicz, I. Pastirk, V. V. Lozovoy, and M. Dantus, "Multiphoton intrapulse interference. 1. Control of multiphoton processes in condensed phases," J. Phys. Chem. A **106**, 9369-9373 (2002).

74. N. Bloembergen, and P. S. Pershan, "Light waves at the boundary of nonlinear media," Phys. Rev. **128**, 606-622 (1962).

75. K. Bahlmann, P. T. So, M. Kirber, R. Reich, B. Kosicki, W. McGonagle, and K. Bellve, "Multifocal multiphoton microscopy (MMM) at a frame rate beyond 600 Hz," Opt. Express **15**, 10991-10998 (2007).

76. V. Iyer, T. M. Hoogland, and P. Saggau, "Fast functional imaging of single neurons using random-access multiphoton (RAMP) microscopy," J. Neurophysiol. **95**, 535-545 (2006).

77. Z. Bor, "Distortion of femtosecond pulses in lenses," Opt. Lett. **14**, 119-121 (1989).

78. M. Kempe, and W. Rudolph, "Impact of chromatic and spherical aberration on the focusing of ultrashort light pulses by lenses," Opt. Lett. **18**, 137-139 (1993).

79. J. B. Guild, C. Xu, and W. W. Webb, "Measurement of group delay dispersion of high numerical aperture objective lenses using two-photon excited fluorescence," Appl. Opt. (1997).

80. M. Muller, J. Squier, R. Wolleschensky, U. Simon, and G. J. Brakenhoff, "Dispersion pre-compensation of 15 femtosecond optical pulses for high-numerical-aperture objectives," J. Microsc. **191**, 141-150 (1998).

81. J. Jasapara, and W. Rudolph, "Characterization of sub-10-fs pulse focusing with high-numerical-aperture microscope objectives," Opt. Lett. **24**, 777-779 (1999).

82. R. L. Fork, C. H. B. Cruz, P. C. Becker, and C. V. Shank, "Compresion of optical pulses to six femtoseconds by cubic phase compensation," Opt. Lett. **12**, 483-485 (1987).

83. G. J. Brakenhoff, M. Muller, and J. Squier, "Femtosecond pulse width control in microscopy by two-photon absorption autocorrelation," J. Microsc. **179**, 253-260 (1995).

84. V. Iyer, B. E. Losavio, and P. Saggau, "Compensation of spatial and temporal dispersion for acousto-optic multiphoton laser-scanning microscopy," J. Biomed. Opt. **8**, 460-471 (2003).

85. F. X. Kartner, U. Morgner, R. Ell, T. Schibli, J. G. Fujimoto, E. P. Ippen, V. Scheuer, G. Angelow, and T. Tschudi, "Ultrabroadband double-chirped mirror pairs for generation of octave spectra," J. Opt. Soc. Am. B **18**, 882-885 (2001).

86. F. X. Kartner, N. Matuschek, T. Schibli, U. Keller, H. A. Haus, C. Heine, R. Morf, V. Scheuer, M. Tilsch, and T. Tschudi, "Design and fabrication of double-chirped mirrors," Opt. Lett. **22**, 831-833 (1997).

87. J.-C. M. Diels, J. J. Fontaine, I. C. McMichael, and F. Simoni, "Control and measurement of ultrashort pulse shapes (in amplitude and phase) with femtosecond accuracy," Appl. Opt. **24**, 1270-1282 (1985).

88. J. K. Ranka, A. L. Gaeta, A. Baltuska, M. S. Pshenichnikov, and D. A. Wiersma, "Autocorrelation measurement of 6-fs pulses based on the two-photon-induced photocurrent in a GaAsP photodiode," Opt. Lett. **22**, 1344-1346 (1997).

89. R. Trebino, and D. J. Kane, "Using phase retrieval to measure the intensity and phase of ultrashort pulses: frequency resolved optical gating," J. Opt. Soc. Am. A **10**, 1101-1111 (1993).

90. R. Trebino, *Frequency-resolved Optical Gating: The Measurement of Ultrashort Laser Pulses* (Kluwer Academic Publishers, Boston, 2000).

91. C. Iaconis, and I. A. Walmsley, "Spectral phase interferometry for direct electric-field reconstruction of ultrashort optical pulses," Opt. Lett. **23**, 792-794 (1998).

92. L. Gallmann, D. H. Sutter, N. Matuschek, G. Steinmeyer, U. Keller, C. Iaconis, and I. A. Walmsley, "Characterization of sub-6-fs optical pulses with spectral phase interferometry for direct electric-field reconstruction," Opt. Lett. **24**, 1314-1316 (1999).

93. M. Kempe, and W. Rudolph, "Femtosecond pulses in the focal region of lenses," Phys. Rev. A **48**, 4721-4729 (1993).

94. T. A. Planchon, S. Ferre, G. Hamoniaux, G. Cheriaux, and J.-P. Chambaret, "Experimental evidence of 25-fs laser pulse distortion in singlet beam expanders," Opt. Lett. **29**, 2300-2302 (2004).

95. M. Kempe, U. Stamm, B. Wilhelmi, and W. Rudolph, "Spatial and temporal transformation of femtosecond laser pulses by lenses and lens systems," J. Opt. Soc. Am. B **9**, 1158-1165 (1992).

96. M. F. Yanik, H. Cinar, H. N. Cinar, A. D. Chisholm, Y. Jin, and A. Ben-Yakar, "Neurosurgery: functional regeneration after laser axotomy," Nature **432**, 822 (2004).

97. I. Maxwell, S. Chung, and E. Mazur, "Nanoprocessing of subcellular targets using femtosecond laser pulses," Med. Laser. App. **20**, 193-200 (2005).

98. A. Uchugonova, K. Konig, R. Bueckle, A. Isemann, and G. Tempea, "Targeted transfection of stem cells with sub-20 femtosecond laser pulses," Opt. Express **16**, 9357-9364 (2008).

99. P. Friedl, "Dynamic imaging of cellular interactions with extracellular matrix," Histochem. Cell Biol. **122**, 183-190 (2004).

100. K. J. Bayless, and G. E. Davis, "Sphingosine-1-phosphate markedly induces matrix metalloproteinase and integrin-dependent human endothelial cell invasion and lumen formation in three-dimensional collagen and fibrin matrices," Biochem. Biophys. Res. Commun. **312**, 903-913 (2003).

101. C. Xu, and W. W. Webb, "Measurement of two-photon excitation cross sections of molecular fluorophores with data from 690 to 1050 nm," J. Opt. Soc. Am. B **13**, 481-491 (1996).

102. C. Xu, W. R. Zipfel, J. B. Shear, R. M. Williams, and W. W. Webb, "Multiphoton fluorescence excitation: new spectral windows for biological nonlinear microscopy," Proc. Natl. Acad. Sci. USA **93**, 10763-10768 (1996).

103. F. Bestvater, E. Spiess, G. Stobrawa, M. Hacker, T. Feurer, R. Porwol, U. Berchner-Pfannschmidt, C. Wotzlaw, and H. Acker, "Two-photon fluorescecne absorption and emission spectra of dyes relevant for cell imaging," J. Microsc. **208**, 108-115 (2002).

104. T. Maciag, J. Cerundolo, S. Ilsley, P. R. Kelley, and R. Forand, "An endothelial cell growth factor from bovine hypothalamus: identification and partial characterization," Proc. Natl. Acad. Sci. USA **76**, 5674-5678 (1979).

105. A. T. Yeh, B. Kao, W. G. Jung, Z. Chen, J. S. Nelson, and B. J. Tromberg, "Imaging wound healing using optical coherence tomography and multiphoton microscopy in an *in vitro* skin-equivalent tissue model," J. Biomed. Opt. **9**, 248-253 (2004).

106. G. P. Agrawal, *Applications of Nonlinear Fiber Optics* (Academic Press, Boston, 2008).

107. G. P. Agrawal, *Nonlinear Fiber Optics* (Acadmic Press, San Diego, 2007).

108. D. G. Ouzounov, K. D. Moll, M. A. Foster, W. R. Zipfel, W. W. Webb, and A. L. Gaeta, "Delivery of nanojoule femtosecond pulses through large-core microstructured fibers," Opt. Lett. **27**, 1513-1515 (2002).

109. S. Ramachandran, M. F. Yan, J. Jasapara, P. Wisk, S. Ghalmi, E. Monberg, and F. V. Dimarcello, "High-Energy (nanojoule) femtosecond pulse delivery with record dispersion higher-order mode fiber," Opt. Lett. **30**, 3225-3227 (2005).

110. S. W. Clark, F. O. Ilday, and F. W. Wise, "Fiber delivery of femtosecond pulses from a Ti:sapphire laser," Opt. Lett. **26**, 1320-1322 (2001).

111. S. H. Lee, A. L. Cavalieri, D. M. Fritz, M. Myaing, and D. A. Reis, "Adaptive dispersion compensation for remote fiber delivery of near-infrared femtosecond pulses," Opt. Lett. **29**, 2602-2604 (2004).

112. M. Lelek, E. Suran, F. Louradour, A. Barthelemy, B. Viellerobe, and F. Lacombe, "Coherent femtosecond pulse shaping for the optimization of a non-linear micro-endoscope," Opt. Express **15**, 10154-10162 (2007).

113. B. Rozsa, G. Katona, E. S. Vizi, Z. Varallyay, A. Saghy, L. Valenta, P. Maak, J. Fekete, A. Banyasz, and R. Szipocs, "Random access three-dimensional two-photon microscopy," Appl. Opt. **46**, 1860-1865 (2007).

114. P. Stoller, B.-M. Kim, A. M. Rubenchik, K. M. Reiser, and L. B. Da Silva, "Polarization-dependent optical second-harmonic imaging of rat-tail tendon," J. Biomed. Opt. **7**, 205-214 (2002).

VITA

Adam M. Larson

Address:
ThorLabs Inc.
435 Rt. 206N
Newton, NJ 07860

Education:
Bachelor of Science (May 2003), Biomedical Engineering concentrating in Optics
University of Rochester, Rochester NY 14627

Doctor of Philosophy (December 2008), Biomedical Engineering
Texas A&M University, College Station TX, 77843

Publications:
A. M. Larson, A. Lee, P. Lee, K. J. Bayless, A. T. Yeh, "Ultrtashort pulse multispectral nonlinear optical microscopy," *in submission*

A. M. Larson and A. T. Yeh, "Delivery of sub-10-fs pulses for nonlinear optical microscopy by polarization-maintaining single mode optical fiber," *Opt. Express* **16**, 14723-14730 (2008)

A. T. Yeh, H. Gibbs, J. Hu, and A. M. Larson, "Advances in nonlinear optical microscopy for visualizing dynamic tissue properties in culture," *Tissue Eng. B. Rev* **14**, 119-129 (2008)

A. M. Larson and A. T. Yeh, "*Ex vivo* characterization of sub-10-fs pulses," *Opt. Lett.* **31**, 1681-1683 (2006)